Sustainable Energy & Fuels

Mesoscopic analyses of the morphology and operation conditions on the transport resistances in a proton-exchange-membrane fuel-cell catalyst layer

Journal:	*Sustainable Energy & Fuels*
Manuscript ID	SE-ART-04-2020-000560
Article Type:	Paper
Date Submitted by the Author:	08-Apr-2020
Complete List of Authors:	MU, YUTONG; Xi'an Jiaotong University, School of Human Settlement and Civil Engineering Weber, Adam; Lawrence Berkeley National Laboratory, Energy Technologies Area Gu, Zhaolin; Xi'an Jiaotong University, School of Human Settlement and Civil Engineering Schuler, Tobias; Lawrence Berkeley National Laboratory, Energy Technologies Area Tao, Wenquan; Xi'an Jiaotong University, School of Energy and Power Engineering

Mesoscopic analyses of the morphology and operation conditions on the transport resistances in a proton-exchange-membrane fuel-cell catalyst layer

Yu-Tong Mu [a*], Adam Z. Weber [b], Zhao-Lin Gu [a], Tobias Schuler [b], Wen-Quan Tao [c]

a. School of Human Settlements and Civil Engineering, Xi'an Jiaotong University, Xi'an, Shaanxi, 710054, China

b. Energy Conversion Group, Energy Technologies Area, Lawrence Berkeley National Laboratory, 1 Cyclotron Road, Berkeley, CA 94720, USA

c. Key Laboratory of Thermo-Fluid Engineering and Science of MOE, School of Energy and Power Engineering, Xi'an Jiaotong University, Xi'an, Shaanxi, 710049, China

*Corresponding email: yutongmu@mail.xjtu.edu.cn

Abstract:

Exploring the origins of local transport resistance and characterizing the oxygen transport resistances in catalyst layer (R_{CL}) are critical for cost reduction. In this paper, a comprehensive mesoscopic model for simulating coupled transport processes of oxygen and water vapor for different structural parameters under different operation conditions in reconstructed microstructures is proposed. The local transport resistance is calculated after achieving the limiting current density. Results demonstrate that R_{CL} increases greatly with decreasing platinum loading (L_{Pt}) and the transport resistances in other components of the cell dominate for high-loadings. Both the reduced oxygen permeation coefficient in ionomer thin-film and the adsorption resistance account for the origins of local transport resistance. The local transport resistance increases with bare carbon ratio for constant L_{Pt} and Pt/C ratio due to the decreased effective ionomer surface, and increases with I/C ratio due to the increased ionomer thickness and decreased Knudsen diffusivity. Due to the presence of liquid water, a slight decrease followed by an increase of the local transport resistance versus relative humidity is obtained. The contribution of ionomer thin-film to R_{CL} is more sensitive to liquid saturation compared with decreased diffusivity of the pores.

Keywords: PEMFC; Local transport resistance; Interfacial resistance; Structural parameters; MRT-lattice Boltzmann method; Liquid water

1. Introduction

The past two decades have witnessed a surge in the substantial research and tremendous development of proton-exchange-membrane fuel cells (PEMFCs) due to their remarkable high power density at a comparatively low operating temperature [1]. Of particular interest is the cost reduction of PEMFCs to accelerate their worldwide commercialization [2]. Curtailing the amount of the platinum-group-metal in the membrane-electrode-assembly (MEA) has triggered an avalanche of activities in catalyst-layer (CL) research [3]. The US Department of Energy set a technical target of the platinum loading (L_{Pt}) of 0.125 mg□cm^{-2} for light-duty vehicles by 2020 [4], while the state-of-the-art L_{Pt} is still around 0.2 to 0.3 mg□cm^{-2} [5]. To achieve this low-loading goal, researchers have proposed many innovative approaches to increase the area specific activity and Pt dispersion by developing new deposition techniques to obtain Pt alloy [6], core-shell [7], and nano-frame electrocatalysts [8]. Highly promising achievements have been achieved at low current densities in ex-situ rotating-disk-electrode studies [9]. However, their benefits at the MEA level are currently under debate with only a few published results on their performance at high current densities [2].

Usually, PEMFCs operate at high current densities to improve the power density and decrease the stack size and consequently investment cost. Nevertheless, as widely reported in several critical reviews [2, 3, 10], unacceptable performance loss due to the vexing rise in mass-transport resistance accompanying low L_{Pt} has been repeatedly demonstrated. Detailed analyses revealed that a local transport resistance $R_{O_2}^{Pt}$ ranging from 100 to 1000 s□m^{-1} accounts for the voltage degradation [11], possibly due to the oxygen transport through the ionomer thin-film [10]. Fig. 1 schematically illustrates the complex transport pathways for oxygen in a cathode porous structure consisting of Pt, voids, ionomer, liquid water, and carbon. As seen, within the CL, percolated networks must exist for reactant ingress and product egress. The oxygen transport resistance of CL, R_{CL}, depends on the porous structure, the operation conditions, and the liquid water amount. The resistance can be separated into resistances caused by the bulk diffusion and the non-diffusional one possibly due to the local resistance at the ionomer/pore and Pt/ionomer interfaces [11-14]. Figs. 1(b) and (c) present the detailed local transport process of O_2 permeating from voids to ionomer thin-films before reaching Pt surfaces. Correspondingly, the genesis of $R_{O_2}^{Pt}$ is assumed to stem from the bulk resistance (R_l) of ionomer thin-film, the interfacial resistance at the ionomer/pore interface (R_{dis}) due to the possible limited dissolution rate, and the interfacial resistance at the Pt/ionomer interface (R_{ads}) due to possible surface adsorption [10]. Experimental

quantification of these pertinent resistances would be instructive; however, they are closely coupled and cannot be readily separated [15]. In addition, the intrinsic heterogeneity of the CL structure, in terms of the distributions of the carbon particle size and the ionomer thin-film thickness, makes quantitative analysis difficult [16, 17].

Fig. 1 Schematic illustration of the oxygen transport process in the CL porous structure, (a) oxygen transport in voids; (b) local transport resistances of oxygen in ionomer thin-film; (c) oxygen permeation in ionomer thin-film

Experimental characterization on the morphology of the ionomer thin-film suggested that transport properties of the reactant species in ionomer thin-film are reduced compared to its bulk analogue due to confinement effects and substrate interactions [18]. Changes in its properties such as the surface wettability and water uptake [19], and swelling [20] have been witnessed. Freiberg et al. [21] corrected the H_2/air PEMFC polarization curves at low-loadings with the mass-transport loss obtained with a hydrogen-pump experiment. Little difference among all the curves was observed, indicating the diffusion-dominated origin of $R_{O_2}^{Pt}$. This finding is also supported by Schuler et al. [22] who concluded that the bulk transport resistance contributed over 70% of the local transport resistances. On the contrary, Owejan et al. [12] demonstrated that the interfacial resistances were prominent to account for the additional transport losses, and Pt particle dispersion should be considered to resolve the performance loss apart from the Pt roughness factor (f_{Pt}, the effective electrochemical surface area normalized by the active area). Kudo et al. [14] found that the interfacial resistances were equivalent to the bulk resistance caused by the ionomer thickness of 30 to 70 nm. This conclusion also was reached by Suzuki et al. [13], who experimentally measured the thickness-dependent resistance of the ionomer thin-film in a planar electrode and ascribed the non-zero positive intercept to the interfacial resistance. Shen et al. [23] addressed that the interfacial resistance came from the ionomer/pore interface. However, this is contrary to Liu et al. [24] who argued that the interfacial transport resistance at the ionomer/pore interface did not exist by measuring the thickness-dependent transport resistance on an inert substrate. They suggested that other effect such as anion poisoning at Pt surface was responsible for the additional loss. By measuring the potential-dependent transport resistance in CL, Suzuki et al. [25] attributed $R_{O_2}^{Pt}$ to the sulfonate coverage of the effective Pt surfaces. Molecular-dynamics studies also revealed that the adsorption of the sulfonate groups on Pt surfaces mainly hindered the oxygen transport and reduced its activity [26].

In addition to ionomer thin-film, liquid water in CL may also account for the genesis of $R_{O_2}^{Pt}$. Typically, the water-transport resistance affects the cell performance in two major ways. Under dry conditions, the transport resistance of the produced water vapor keeps the ionomer more humidified, thereby lowering R_I and proton resistance. Under wet or very humid conditions, the vapor may condense, thereby resulting in water flooding that hinders the gas transport pathways [27]. This has been supported by Sui et al. [23], who observed an increasing $R_{O_2}^{Pt}$ with the oxygen fraction, and Nonoyama et al. [28], Shukla et al. [29] and Iden et al. [30], who observed an increasing $R_{O_2}^{Pt}$ with high relative humidity. Muzaffar et al. [31] addressed that the tipping water balance dominated the transport loss as the oxygen permeability and the exchange current density decreased with low L_{Pt}. Mashio et al. [32] and Ono et al. [33] attributed $R_{O_2}^{Pt}$ to two local transport processes caused by the ionomer thin-film and the liquid water.

Apart from the experimental studies, numerical investigations including the agglomerate model and mesoscopic method have been adopted to analyze the transport process in CL. However, the large and random agglomerate size and film thickness in the traditional agglomerate model were not supported in scanning electron micrographs (SEM) [34]. Chowdhury et al. [17] presented an analytical agglomerate model to describe the 1D transport process. The effective ionomer thickness and the active mass-transport area per unit volume were identified as two critical parameters in determining R_{CL}. Schuler et al. [22] further extended the above model to consider the 2D mass-transport by introducing a focusing factor. Interfacial transport resistances were considered in the agglomerate model proposed by Moore et al. [35], Secanell et al. [36], and Suzuki et al. [13]. The micro-scale model termed as the "catalyst coated particle" was combined with a two-phase flow model to analyze the performance of the microporous layer by Zhou et al. [37]. Hao et al. [38] further extended the model to characterize the micro-scale transport resistance by considering the Pt distribution on the agglomerate surface. Nevertheless, most agglomerate models fail to match the experimentally observed trends in exploring the impacts of the structural parameters on R_{CL}[39]. Mesoscopic models are considered to be superior by fully considering the heterogeneous and complex structures of CL. Zhang and Gao [40] explored the impact of liquid water on cell performance. However, their work was actually based on an agglomerate model without distinguishing the components of Pt and carbon. Sabharwal et al. [41] focused on the oxygen transport and chemical reaction processes in CL. However, morphologies of

ionomer and Pt were also not characterized and electrochemical reactions were assumed to occur at all gas/solid surfaces. Cetinbas et al. [16, 42] explored the effective transport properties of CL microstructures obtained with hybrid approaches including the nano-CT, transmission electron microscopy (TEM), and X-ray scattering. Hou et al. [43] investigated the impact of the structural parameters on the cell performance without fully considering the detailed local transport process. Recently, we reported a comprehensive model that can consider the local transport process including the interfacial transport resistances and bulk resistances using the lattice Boltzmann method (LBM) [15]. However, the transport of water in the CL was not included due to the prior focus on the anode CL to match with hydrogen-pump experimental data.

As demonstrated above, the transport processes of oxygen and water are fully coupled. To the best knowledge of the authors, few mesoscopic studies on the local transport resistance of oxygen have considered water transport in detail, limiting their ability to reveal the coupled mechanisms of the local transport behaviors in CL. The objective of the present work therefore is to extend our previous work to consider the electrochemical reaction and transport processes of oxygen and water vapor in a cathode CL, where the impact of liquid water on the transport resistances is considered explicitly. With this model, the coupling of oxygen and water transport processes at the mesoscopic level is achieved. Impacts of the structural parameters together with the operation conditions such as the relative humidity and the molar fraction of oxygen on the transport resistances are explored.

2. Transport resistances and physical model

2.1 Transport resistances

To characterize R_{CL}, a limiting-current measurement is usually employed. The mass-transport limit is achieved by feeding the cathode CL with low amounts of O_2 diluted in other inert species. A high flowrate of the reactant gas mitigates the variation of O_2 concentration along the flow direction. The relative humidity (RH) is a critical operation parameter to clarify the local transport resistance originated from the microstructure itself. Typically, the cell RH is kept under 100% to avoid water condensation, but not too dry to minimize ohmic limitations and the inherent non-uniform distribution of the current density. Limiting current density, i_{lim}, can be obtained by decreasing the output voltage from open

circuit until a constant current density is obtained. As the oxygen concentration at Pt surfaces approaches zero at i_{lim}, the total oxygen transport resistance, R_{tot}, can be calculated as

$$R_{tot} = \frac{4Fc_{O_2}^{in}}{i_{lim}} = R_{CH} + R_{GDL} + R_{CL} \quad (1)$$

where F and $c_{O_2}^{in}$ are Faraday's constant, and the oxygen concentration in channel (CH), respectively. R_{CH} and R_{GDL} denote the oxygen transport resistances in CH and gas diffusion layer (GDL), respectively. Based on a 1D diffusion model considering the electrochemical reaction in the CL, Grezler et al. [11] deduced an analytical correlation to calculate R_{CL},

$$R_{CL} = \frac{R_{O_2}^{Pt}}{f_{Pt}} (l/\psi) \coth(l/\psi) \quad (2)$$

where l is the CL thickness, and the quantity ψ is defined as $\psi = \sqrt{D_{O_2,CL}^{eff} l R_{O_2}^{Pt} / f_{Pt}}$ with $D_{O_2,CL}^{eff}$ denoted as the effective oxygen diffusivity in CL. The term $R_{O_2}^{Pt} / f_{Pt}$ is defined as R_{Film} as it is completely attributed to the ionomer thin-film. Therefore, the contribution of pores R_{Pore} to R_{CL} is calculated as

$$R_{Pore} = R_{Film} \left[(l/\psi) \coth(l/\psi) - 1 \right] \quad (3)$$

One can find that R_{Pore} is closely related to R_{Film}. As l/ψ approaches zero, R_{Pore} can be further simplified with a Taylor-series expansion to

$$R_{Pore} \approx \frac{l}{3D_{O_2,CL}^{eff}} \quad (4)$$

Therefore, Eq. (2) can be expressed as

$$R_{CL} = \frac{l}{3D_{O_2,CL}^{eff}} + \frac{R_{O_2}^{Pt}}{f_{Pt}} \quad (5)$$

According to Eq. (5), a straight line with its slope of $R_{O_2}^{Pt}$ is produced by plotting R_{CL} versus the inverse of f_{Pt}. Nevertheless, typical ways by altering the carbon dilution or l to achieve a set of f_{Pt} may influence $R_{O_2}^{Pt}$ to some extent. For one thing, the cell performance, especially due to the water management, is sensitive to l [44]. Specifically, the water content λ in CL may differ with l greatly, resulting in different R_I as λ affects the transport properties of

O_2 in the ionomer. For another, $R_{O_2}^{Pt}$ may be affected by Pt dispersion on the Pt/C mixture, which has been evidenced by Owejan et al. [12] experimentally and Mu et al. [15] numerically. Therefore, the accuracy of the linearly fitted $R_{O_2}^{Pt}$ may be affected. In the present work, $R_{O_2}^{Pt}$ is analytically solved using Eq. (2) with Newton iterative method after $D_{O_2,CL}^{eff}$ and R_{CL} are numerically resolved.

2.2 Physical model

To capture the detailed local transport processes, CL microstructures should be close to the realistic ones as the ionomer morphologies affect the transport of the reactant and proton directly. Cetinbas et al. [16] experimentally found that the primary carbon size ranged from 20 to 75 nm, and the ionomer thickness ranged from 2.5 to 27.5 nm. Due to its merits such as low cost and easy implementation, stochastic generation method has been widely used to reconstruct the CL microstructures [15, 16, 41, 45, 46]. Based on the total components number of the reconstructed CL, physical models with two components (pore and ionomer) [41, 46], three components (pore, ionomer and Pt/C mixture) [16, 45], and four components (pore, ionomer, Pt and carbon) [15] have been proposed. The morphologies reconstructed with our previous method feature a high accordance with the experimental observed ones in terms of the distributions of the primary carbon size and ionomer thickness, and the roughness factor f_{Pt} [15], and therefore it is adopted here.

Prior to the reconstruction, the volume fractions of each components in the CL determined based on the manufacture's specifications, such as the mass fraction of platinum in the supported catalyst (ω), the ratio of ionomer and carbon by mass (γ), the porosity (ε), and the bare carbon fraction by volume (y_{bare}), are calculated as

$$\varepsilon_{Pt} = \frac{L_{Pt}}{l\rho_{Pt}} \tag{6a}$$

$$\varepsilon_C = \left(1 - y_{bare}\right)\left(1 - \varepsilon - \varepsilon_{Pt}\right) \Big/ \left(1 + \frac{\rho_C}{\rho_{ion}}\gamma\right) \tag{6b}$$

$$\varepsilon_{ion} = 1 - \varepsilon - \varepsilon_C / \left(1 - y_{bare}\right) - \varepsilon_{Pt} \tag{6c}$$

where densities of carbon, platinum, and ionomer are given as 1.8, 21.45, and 2 g□cm^{-3},

respectively [15]. Notably, if the simulated water vapor is oversaturated, the liquid component in CL is considered. Details on the calculation of the liquid water saturation will be introduced in the following section.

Fig. 2 depicts the characterization of the reconstructed CL. Let (x,y,z) denote Cartesian coordinates defined such that y and z span the cross-section, and x points along the thickness. x=0 is the CL/GDL interface and x=l is the CL/Membrane interface. Detailed structural parameters of the simulated cases are listed in Table 1, which are based on the experimental work carried out by Grezler et al. [11] and Owejan et al. [12]. Note that the reconstructed CL is more for Pt on Vulcan carbon, where the Pt is on the outside of primary carbon particles. For all simulated cases, a cross-section size of 250×250 nm is assigned with a mesh resolution of 2.5 nm. The minimum size of the simulated Pt particles is 2.5 nm, which is supported by the experimentally observed 2 to 3 nm reported by Guo et al. [47], and 2 nm reported by Cetinbas et al. [16]. As shown in Fig. 2(a), all of the components are distinguished. The primary carbon particles with different sizes are coated with ionomer. Platinum particles are supported on carbons. Note that only the CL thickness ranging from 5.5 to 6.5 μm are shown as the ratio of lengths in thickness direction is about 50 times higher than that in other directions. For better visualization of Pt distributions in CL, we have plotted their locations of cases 3 and 5 in Fig. 2(b). It can be observed that Pt number is higher and almost all of the primary carbons are deposited with Pt particles for case 5. For comparison, only a part of carbon particles is active for the dispersion of Pt particles, maintaining the same ω of Pt/C mixtures for different L_{Pt}. Fig. 3(c) presents the distributions of carbon particle size and ionomer thin-film thickness of case 3. An excellent match between the simulated data and the experimental data carried out by Cetinbas et al. [16] is achieved. The mean size of the primary carbon is around 45 nm, and the mean thickness of the ionomer thin-film is around 7.5 nm. Fig. 2(d) illustrates Pt distributions with the same L_{Pt} of cases 6 and 10. Due to their difference in y_{bare}, ω differs from 5% to 30%. It can be clearly found that the distribution of Pt particles are deposited comparatively uniform for case 6. Based on the above analyses, the present physical models can provide the detailed features of CL microstructures.

The normalized face-average fractions of different components of case 3, defined as the face-average fractions normalized by the volume-average ones, are presented in Fig. 2(e) with

the thickness ranging from 3.5 to 8.5μm. Due to the high ratio of bare carbons diluted in Pt/C mixtures and low volume fraction of Pt particles, the normalized face-average fraction of Pt along the thickness direction differs greatly from 0 to 3.6. This is understandable as the carbon particles are randomly chosen to support Pt particles. For the normalized face-average fraction of 0, it suggests that no Pt particles are deposited at the current cross-section, and thereby no electrochemical reaction occurs. For the rest of the components, only a small variation of the face-average fractions is observed. To explore the local transport resistance accurately, f_{Pt} is a critical parameter as demonstrated in Eq. (2). A statistical integrated Pt surface with their neighboring nodes labelled as ionomer may overestimate f_{Pt} as some of the ionomer may be isolated for proton transport. The inactive surface is excluded with the method introduced in our previous work [15]. As depicted in Fig. 2(f), we have compared the numerical predicted f_{Pt} with the experimental ones given by Grezler et al. [11] and Owejan et al. [12]. It can be observed that the simulated f_{Pt} agrees well with the experimental data. A plot of f_{Pt} versus L_{Pt} produces the Pt-mass-specific electrochemical surface area a_{ECSA}. The respective fitted a_{ECSA} for the simulated data and Grezler's data are 54.8 and 57.4 $m^2 \cdot g_{Pt}^{-1}$, with the relative deviation of 4.5%. The respective fitted a_{ECSA} for the simulated data and Owejan's data are 68.6 and 71.2 $m^2 \cdot g_{Pt}^{-1}$, with the relative deviation of 3.7%. As only L_{Pt} of 0.025mg$\cdot$cm^{-2} is simulated (see cases 6 to 10 in Table 1) and the simulated f_{Pt} varies slightly from 16.93 to 17.27 $m_{Pt}^2 \cdot m_{MEA}^{-2}$, little difference of the simulated f_{Pt} can be observed in Fig. 2(f). Based on the aforementioned analyses, it is reliable to explore the oxygen and vapor transport processes in CL at the mesoscopic level.

Fig. 2 Characterization of the reconstructed CL microstructures, (a) CL morphology of case 3 (void: white, carbon: black, platinum: red; ionomer: cyan); (b) locations of Pt particles for different L_{Pt} of cases 3 and 5; (c) comparison of the distributions of carbon particle size and ionomer thin-film thickness between the simulated and experimental data [16] of case 3; (d) locations of Pt particles for different y_{bare} of cases 6 and 10; (e) normalized face-average fractions of the components along the thickness direction of case 3; (f) comparison of f_{Pt} between the simulated cases and experimental data [11, 12]

Table 1. Structural parameters of the simulated cases

3. Numerical methodology

3.1 Governing equations

To analyze the coupling effect of oxygen and vapor transport processes in CL, both the governing equations of oxygen and vapor concentrations are considered. The mathematical model is subject to the following assumptions:

(1) Only the cathode CL is considered, which operates at steady-state.

(2) The CL is formed by a mixture of carbon, Pt, ionomer thin-film, and pore void. Liquid water exists if the vapor concentration is oversaturated. Electrochemical reactions only occur at the ionomer/Pt surfaces.

(3) Gas convection in CL is neglected, and the transport resistance of oxygen from CH to CL/GDL interface, $R_{O2,\ CH+GDL}$, is given based on the experimental results of Grezler et al. [11]. Correspondingly, $R_{H2O,\ CH+GDL}$ is calculated based on the ratio of molecular diffusion coefficients of oxygen and vapor.

(4) The water content in ionomer thin-film during the whole transport process is assumed to be in equilibrium with the local water activity. Liquid water saturation, defined as the total nodes of the liquid water divided by the total nodes of the initial pore voids, is iteratively calculated based on the liquid water flux governed by the capillary driven flow.

(5) Isothermal assumption is used as the current density is comparatively small due to the low-concentration of oxygen [48].

(6) As pointed out by Yoon and Weber [48], isopotential assumption for proton is valid if the proton conductivity is above 10^{-2} S□m^{-1}, which is about two order-of-magnitude lower than that adopted in the present study. Detailed validation on this assumption can be found in SI.

3.1.1 Oxygen transport

In CL, oxygen transports in the pore voids, ionomer thin-films, and the liquid water before reaching Pt surfaces. At the interfaces of pore and ionomer, a possible limited dissolution rate of oxygen may exist. At the interfaces of ionomer and Pt, a possible limited adsorption rate may exist. At the interfaces of ionomer and liquid water, the partial pressure of oxygen should be the same. At the interfaces of ionomer and Pt, electrochemical reaction

occurs. To characterize the above processes, equations for the oxygen transporting in pores, ionomer and liquid water are expressed as

$$\nabla \cdot \left(D_{\mathrm{p,O_2}} \nabla c_{\mathrm{p,O_2}} \right) = 0 \tag{7a}$$

$$\nabla \cdot \left(D_{\mathrm{ion,O_2}} \nabla c_{\mathrm{ion,O_2}} \right) = 0 \tag{7b}$$

$$\nabla \cdot \left(D_{\mathrm{liq,O_2}} \nabla c_{\mathrm{liq,O_2}} \right) = 0 \tag{7c}$$

where the subscripts of p, ion, and liq represent pores, ionomer and liquid water, respectively, and D is the diffusion coefficient. Owing to the solubility difference of oxygen in pores and ionomer or liquid water and the possible limited dissolution rate $k_{\mathrm{ion,dis}}$ or $k_{\mathrm{liq,dis}}$ (m□s^{-1}), conjugated boundary conditions at the corresponding interfaces yield

$$-D_{\mathrm{p,O_2}} \frac{\partial c_{\mathrm{p,O_2}}}{\partial n} = -D_{\mathrm{ion,O_2}} \frac{\partial c_{\mathrm{ion,O_2}}}{\partial n} = k_{\mathrm{ion,dis}} \left(c^{\mathrm{eq}}_{\mathrm{ion,O_2}} - c_{\mathrm{ion,O_2}} \right) \tag{8a}$$

$$-D_{\mathrm{p,O_2}} \frac{\partial c_{\mathrm{p,O_2}}}{\partial n} = -D_{\mathrm{liq,O_2}} \frac{\partial c_{\mathrm{liq,O_2}}}{\partial n} = k_{\mathrm{liq,dis}} \left(c^{\mathrm{eq}}_{\mathrm{liq,O_2}} - c_{\mathrm{liq,O_2}} \right) \tag{8b}$$

$$-D_{\mathrm{liq,O_2}} \frac{\partial c_{\mathrm{liq,O_2}}}{\partial n} = -D_{\mathrm{ion,O_2}} \frac{\partial c_{\mathrm{ion,O_2}}}{\partial n}, \; H_{\mathrm{liq}} c^{\mathrm{eq}}_{\mathrm{liq,O_2}} = H c^{\mathrm{eq}}_{\mathrm{ion,O_2}} \tag{8c}$$

where ***n*** denotes the unit normal vector perpendicular to the interfaces of pore and ionomer or liquid water pointing toward the pores. $c_{\mathrm{p,O2}}$ is the oxygen concentration in pores at the interfaces of pore and ionomer or liquid water. Equilibrium oxygen concentrations at ionomer/liquid at the interfaces of pore and ionomer or liquid are calculated as

$$c^{\mathrm{eq}}_{\mathrm{ion,O_2}} = RTc_{\mathrm{p,O_2}} / H \tag{9a}$$

$$c^{\mathrm{eq}}_{\mathrm{liq,O_2}} = RTc_{\mathrm{p,O_2}} / H_{\mathrm{liq}} \tag{9b}$$

where R and T are the universal gas constant and absolute temperature, respectively. The Henry constant H (Pa□m^{-3}mol^{-1}) is obtained with [13]

$$H = 101325 / \left(4.408 - 0.09712\lambda \right) \tag{10}$$

with the water content λ calculated as a function of the water activity a [49],

$$\lambda = 0.043 + 17.18a - 39.85a^2 + 36a^3 \quad \left(a = p_{\mathrm{vp}} / p_{\mathrm{sat}} \right) \tag{11}$$

where the respective p_{vp} and p_{sat} denote the partial pressure of vapor and saturation pressure.

The diffusivity of oxygen in the bulk ionomer $D_{\text{ion,O2}}$ ($m^2 \cdot s^{-1}$) is calculated from the data fit for a bulk ionomer [13],

$$D_{\text{ion},O_2} = 1.14698 \times 10^{-10} \lambda^{0.708} \tag{12}$$

The bulk permeation coefficient, ψ_0, is calculated with the oxygen diffusivity in the bulk ionomer divided by the Henry constant. To distinguish the permeation coefficient of the bulk ionomer from that of the ionomer thin-film, we define ψ_{O2} as the permeation coefficient of the ionomer thin-film. The oxygen diffusivity in the ionomer thin-film is reduced compared to its bulk analogue to mimic the confined effect.

The oxygen diffusivity in pores $D_{\text{p,O2}}$ is locally specified as a function of pore diameter d_p as the characteristic size of pores is close to the mean free path of gas molecules. It is determined with a simple form of the Bosanquet formula,

$$D_{\text{p},O_2} = \left(D_{\text{Kn},O_2}^{-1} + D_{O_2:\text{mix}}^{-1} \right)^{-1} \tag{13}$$

with the Knudsen diffusivity $D_{\text{Kn, O2}}$ ($m^2 \cdot s^{-1}$) calculated as

$$D_{\text{Kn},O_2} = \frac{d_p}{3} \sqrt{\frac{8RT}{\pi M_{O_2}}} \tag{14}$$

where M is the gas molecular weight. The molecular diffusivity $D_{\text{O2:mix}}$ ($m^2 \cdot s^{-1}$) for a binary mixture of gases is calculated as [50],

$$D_{O_2:\text{mix}} = \left(\frac{y_{H_2O}}{D_{O_2:H_2O}} + \frac{y_{N_2}}{D_{O_2:N_2}} \right)^{-1} \tag{15a}$$

$$D_{O_2:H_2O/N_2} = \frac{0.0000001 T^{1.75}}{P\left(v_{O_2}^{1/3} + v_{H_2O/N_2}^{1/3} \right)^2} \left(M_{O_2}^{-1} + M_{H_2O/N_2}^{-1} \right)^{0.5} \tag{15b}$$

where P, y and v are the total pressure (atm), mole fraction, and the diffusion volume of species, respectively. In the present study, the diffusion volumes are 16.6, 17.9, and 12.7 nm^3 for O_2, N_2, and H_2O, respectively [50].

Owing to the electrochemical reaction and possible limited adsorption rate k_{ads} ($m \cdot s^{-1}$), conjugated boundary conditions at the active Pt/ionomer interfaces yield

$$-D_{\text{ion},O_2} \frac{\partial c_{\text{ion},O_2}}{\partial n} = k_{\text{ads}} \left(c_{\text{ion},O_2} - c_{\text{Pt},O_2} \right) = j/4F \tag{16}$$

where $\boldsymbol{n}$ denotes the unit normal vector perpendicular to Pt/ionomer interface pointing toward

the ionomer, $c_{Pt,O2}$ is the adsorbed oxygen concentration at Pt surfaces. The chemical reaction rate j (A□m^{-2}) related to $c_{Pt,O2}$ and the oxide coverage effect is given in SI.

3.1.2 Water transport

In the CL, the water vapor and the membrane water transport in the pore voids and the ionomer thin-film, respectively. The liquid water transports in the pores due to the capillary effect. To describe the above processes, equations for the water transport in pores and ionomer thin-film are expressed as

$$\nabla \cdot \left(D_{\mathrm{p,\,H_2O}} \nabla c_{\mathrm{p,\,H_2O}} \right) = 0 \tag{17a}$$

$$\nabla \cdot \left(D_{\mathrm{ion,H_2O}} \nabla c_{\mathrm{ion,H_2O}} \right) = 0 \tag{17b}$$

Conjugated boundary conditions at the ionomer/pore interfaces for water transport are

$$-D_{\mathrm{p,\,H_2O}} \frac{\partial c_{\mathrm{p,\,H_2O}}}{\partial n} = -D_{\mathrm{ion,H_2O}} \frac{\partial c_{\mathrm{ion,H_2O}}}{\partial n}, \quad c_{\mathrm{ion,H_2O}} = c_{\mathrm{p,\,H_2O}} \tag{18}$$

The diffusivity of water vapor $D_{ion,H2O}$ (m^2□s^{-1}) is calculated as [51]

$$D_{\mathrm{ion,H_2O}} = 4.17 \times 10^{-8} \left[161 \exp(-\lambda) + 1 \right] \exp\left[\frac{-2346}{T} \right] \quad (3<\lambda<17) \tag{19}$$

Similar to $D_{p,O2}$, the vapor diffusivity in pores $D_{p,H2O}$ is locally specified. Owing to the electrochemical reaction at the Pt/ionomer interfaces, the conjugated boundary condition is specified as

$$-D_{\mathrm{ion,H_2O}} \frac{\partial c_{\mathrm{ion,H_2O}}}{\partial n} = -S_{\mathrm{H_2O}} \tag{20}$$

where ***n*** denotes the unit normal vector perpendicular to Pt/ionomer interface pointing toward the ionomer. S_{H2O} (mol□m^{-2}s^{-1}) is defined as the source term of the membrane water. Obviously, it equals $j/2F$ without considering additional water fluxes caused by the electro-osmosis drag (EOD), the vapor concentration gradient (VCG), and the liquid pressure gradient (LPG).

The water flux from anode to cathode by the hydrogen ions due to EOD is given as $S_{EOD}=n_d\, j/F$ with the electro-osmotic coefficient (n_d) calculated as $n_d=2.5\lambda/22$ [49]. The membrane water flux transporting from cathode to anode, S_{MW} (mol□m^{-2}s^{-1}), can be expressed by

$$S_{\mathrm{MW}}=D_{\mathrm{ion,H2O}}\frac{\rho_{\mathrm{mem}}}{EW}\frac{\left(\bar{\lambda}_{\mathrm{CCL}}-\bar{\lambda}_{\mathrm{ACL}}\right)}{\delta_{\mathrm{mem}}} \tag{21}$$

where ρ_{mem}, EW, $\bar{\lambda}_{\mathrm{CCL}}$, and $\bar{\lambda}_{\mathrm{ACL}}$ denote to the density of dry membrane, equivalent weight of membrane, and the mean membrane water content in cathode and anode, respectively. As only the cathode CL is simulated in the present work, $\bar{\lambda}_{\mathrm{ACL}}$ is assumed to be in equilibrium with the inlet water activity. As there is no source term of the water content in membrane, linear distribution of water content along the thickness direction is expected. $D_{\mathrm{ion,H2O}}$ is specified with Eq. (19) with the water content chosen as an average of $\bar{\lambda}_{\mathrm{CCL}}$ and $\bar{\lambda}_{\mathrm{ACL}}$.

The water flux due to the vapor concentration gradient, S_{VCG} (mol□m^{-2}s^{-1}), can be expressed by

$$S_{\mathrm{VCG}}=\begin{cases}\left(c_{\mathrm{H_2O,CCL/GDL}}-c_{\mathrm{H_2O}}^{\mathrm{in}}\right)\Big/R_{\mathrm{H_2O,CH+GDL}} & \text{if } c_{\mathrm{H_2O,CCL/GDL}}\le c_{\mathrm{sat}}^{0}\\ \left(c_{\mathrm{sat}}-c_{\mathrm{H_2O}}^{\mathrm{in}}\right)\Big/R_{\mathrm{H_2O,CH+GDL}} & \text{if } c_{\mathrm{H_2O,CCL/GDL}}>c_{\mathrm{sat}}^{0}\end{cases} \tag{22}$$

where the inlet concentration of vapor in CH, $c_{\mathrm{H_2O}}^{\mathrm{in}}$, is calculated based on the operating conditions. The saturation vapor concentration, c_{sat}, is corrected for the pore effects by the Kelvin equation [52],

$$c_{\mathrm{sat}}=c_{\mathrm{sat}}^{0}\exp\left(p_{\mathrm{c,CL}}\bar{V}_{\mathrm{w}}/RT\right) \tag{23}$$

where c_{sat}^{0} is the uncorrected vapor concentration, $p_{\mathrm{c,CL}}$ is the capillary pressure of the CL, and $\bar{V}_{\mathrm{w}}$ is the molar volume of water.

The water flux due to the liquid pressure gradient, S_{LPG} (mol□m^{-2}s^{-1}), is calculated with [53],

$$S_{\mathrm{LPG}}=\rho_{\mathrm{liq}}\frac{K_{\mathrm{GDL}}k_{\mathrm{liq}}}{\mu_{\mathrm{liq}}M_{\mathrm{H_2O}}}\frac{\left(\bar{p}_{\mathrm{liq,\,CL}}-\bar{p}_{\mathrm{liq,\,CH}}\right)}{\delta_{\mathrm{GDL}}} \tag{24}$$

where ρ_{liq}, K_{gdl}, k_{liq}, μ_{liq}, δ_{gdl}, $\bar{p}_{\mathrm{liq,\,CL}}$, and $\bar{p}_{\mathrm{liq,\,CH}}$ denote the density of liquid water, the intrinsic permeability of GDL, the liquid phase permeability, the dynamic viscosity of liquid water, the GDL thickness, and the liquid pressure of cathode CL and CH, respectively. As the stoichiometry ratio is high and the current density is low, the liquid saturation s_{CH} in CH is

assumed to be 0. k_{liq} is related to s as $k_{liq}=s^3$ [53]. According to the Leverett-J function, p_{lid} can be calculated as [49],

$$p_{liq} = p_g - p_c = p_g - \sigma\cos\theta\left(\frac{\varepsilon}{K}\right)^{0.5} J(s) \tag{25a}$$

$$J(s) = 1.42s - 2.12s^2 + 1.26s^3 \quad \text{for } \theta > 90° \tag{25b}$$

where σ is the surface tension, θ is the contact angle, and p_g is the gas phase pressure. In the present work, p_g is assumed to be a constant. The liquid saturation of GDL at the interface of CL/GDL, $s_{CL/GDL}$, can be easily determined as the liquid pressure at the interface is continuous, i.e., $\overline{p}_{liq,\,CL} = p_{liq,\,CL/GDL}$. The saturation used to determine k_{liq} is obtained by averaging $s_{CL/GDL}$ and s_{CH}. Based on the water flux balance, we have

$$\sum_k \frac{(n_d + 0.5) j_k \delta^2 x}{F} = (S_{MW} + S_{LPG} + S_{VCG}) A_{CL} = (S_{MW} + S_{LPG}) A_{CL} + \sum_k S_{H2O,k} \delta^2 x \tag{26}$$

where $\delta^2 x$ is the local active electrochemical area, A_{CL} is the CL cross-section area, and the current density, i, is calculated by integrating the surface reaction rate j_k over all the reaction surfaces and then normalized by A_{CL}, i.e., $i = \sum_k j_k \delta^2 x \Big/ A_{CL}$. Combined with Eqs. (21~26), all the water fluxes can be solved by using Newton iterative method. The local water source term S_{H2O} is expressed as

$$S_{H_2O,k} = j_k \left(\frac{n_d + 0.5}{F} - \frac{S_{MW} + S_{LPG}}{i}\right) \tag{27}$$

Notably the source term is only present at the active Pt/ionomer surfaces where the electrochemical reaction occurs. All the model parameters used in this section are summarized in Table 2. Given the lack of relevant data for $k_{ion,dis}$ and $k_{liq,dis}$, and based on the experimental results provided by Liu et al. [24] and Suzuki et al. [25], they are specified as infinitely large in the present work. To solve the above governing equations, as well as the conjugated boundary conditions at mesoscopic level, the multiple-relaxation-time (MRT) LBM are adopted [15, 54]. Details can be found in SI.

Table 2. Parameters for the electrochemical kinetics and the model [32, 38, 49]

3.2 Boundary conditions and solution strategy

Due to the transport resistances of oxygen and vapor caused by CH and GDL, the oxygen and vapor concentrations at x=0 varies with current density as their concentrations in CH are determined based on the operation conditions. The simulated operation conditions are x_{O2}=1%, T=353.15K, and p=110 kPa for the cases listed in Table 1. RH=62% for cases 1 to 5 based on Grezler's experiement [11], and RH=80% for cases 6 to 10 based on Owejan's experiment [12]. The sum of R_{CH} and R_{GDL} for the oxygen transport is chosen as 46 s□m^{-1} based on the experimental data [11], and that for the vapor transport is given as 37.8 s□m^{-1} based on the ratio of molecular diffusion coefficients of oxygen and vapor. Numerical implementation for the oxygen and vapor transport processes at x=0 are specified as

$$f_1\left(\mathbf{x}, t+\delta t\right)=\frac{\left(\varepsilon_{\mathrm{D}} R_{\mathrm{O}_2,\,\mathrm{CH+GDL}}-1\right)\hat{f}_2\left(\mathbf{x}, t\right)+\varepsilon_{\mathrm{D}} c_{\mathrm{O}_2}^{\mathrm{in}}}{\varepsilon_{\mathrm{D}} R_{\mathrm{O}_2,\,\mathrm{CH+GDL}}+1} \tag{28a}$$

$$g_1\left(\mathbf{x}, t+\delta t\right)=\frac{\left(\varepsilon_{\mathrm{D}} R_{\mathrm{H_2O},\,\mathrm{CH+GDL}}-1\right)\hat{g}_2\left(\mathbf{x}, t\right)+\varepsilon_{\mathrm{D}} c_{\mathrm{H_2O}}^{\mathrm{in}}}{\varepsilon_{\mathrm{D}} R_{\mathrm{H_2O},\,\mathrm{CH+GDL}}+1} \tag{28b}$$

where the inlet concentrations of oxygen and vapor $c_{\mathrm{O}_2}^{\mathrm{in}}$ and $c_{\mathrm{H_2O}}^{\mathrm{in}}$ in CH are calculated based on the operating conditions. Details on the distribution populations **f**(**x**, t) and **g**(**x**, t) can be found in SI. Half-lattice, bounce-back condition is implemented at x=l as the membrane is impermeable for oxygen and vapor. Periodic conditions are implemented at the y- and z-directions, enabling our model to simulate a sufficiently large cross-section. A detailed simulation flowchart can be found in Fig. S2.

It is expected that the vapor concentration in CL may probably surpass the saturated concentration if the inlet RH or x_{O2} is sufficiently high. In this case, the liquid condensation may occur. To characterize the liquid saturation in CL for each time step, the liquid flux needs to be known first. By using the water fluxes S_{MW} and S_{VCG} calculated in the last time step, the liquid water flux S_{LPG} at the current time step can be obtained with Eq. (26). Then, the liquid saturations in CL and GDL, s_{CL} and s_{GDL}, can be iteratively calculated using Eqs. (24) and (25). Except for the liquid saturations, the saturation vapor concentration c_{sat} is updated at the current time step. Owing to the vapor-phase transporting in CL, the vapor concentration in pores only changes slightly (see Fig. S3). Therefore, liquid condensation occurs throughout the layer, not merely at the reaction sites. The movement of the liquid water and the kinetics

of evaporation and condensation are beyond the scope of the current study that focuses on the transport resistances. Pores with their neighboring nodes labeled as non-pores will be assigned as liquid water based on a small probability c_d and the calculated s_{CL}. Since the newly inserted liquid water will affect the oxygen transport and the current density, the real liquid saturation increases gradually to maintain its numerical stability. For example, we only add 1% of $s_{CL}\varepsilon N_x N_y N_z$ every 2000 time steps with N_x, N_y, and N_z denoting to the nodes in *x*-, *y*- and *z*- directions. The simulation will not stop until the relative variation of the current density is smaller than 10^{-5} every 2000 time steps.

4. Results and discussion

4.1 Determination of the limiting current density and the effective diffusivity

As addressed in section 2.1, the determination of the transport resistances in CL relies on the limiting current density i_{lim}, and the effective diffusivity of oxygen $D^{eff}_{O_2,CL}$. By altering the cathode overpotential η_c, the polarization curves of CLs with different L_{Pt}, corresponding to cases 1 to 5, are obtained. As seen in Fig. 3, current densities increase with the decrease of the output voltage and then reach a constant. All the curves are insensitive to the output voltage when the voltage is below 0.3V. The maximum current density due to the limited oxygen transport through the ionomer thin-film is considered as i_{lim}. As the thicknesses for all the simulated cases are similar, it is expected that i_{lim} increases with L_{Pt} due to the high f_{Pt}. The respective limiting current densities for L_{Pt} of 0.1, 0.2, and 0.4 mg□cm^{-2} are 3029, 3510, and 3886 A□m^{-2}. It is suggested that i_{lim} only increases 28% despite of the quadruple L_{Pt} from 0.1 to 0.4 mg□cm^{-2}. The reason is as follows: the increased i_{lim} corresponds to higher oxygen concentration loss caused by $R_{O2,CH+GDL}$, hence resulting in lower oxygen concentration at the interfaces of GDL/CL as $c^{in}_{O_2}$ is held constant. This indicates that $R_{O2,CH+GDL}$ dominates in determining the cell performance for high L_{Pt}. A tradeoff between the cell cost and performance needs to be balanced for the CL design. Detailed illustrations of the oxygen concentrations in pores, ionomer, and Pt surfaces, and the vapor concentrations in pores, water content in ionomer, and the surface reaction rate at i_{lim} are provided in Fig. S3.

Fig. 3 Polarization curves of CLs with different L_{Pt}

To assess the validity of the predicted effective oxygen diffusivities $D_{O_2,CL}^{eff}$, the formation factor F, defined as the effective diffusivity normalized by the molecular diffusivity, is used. Three sets of the reconstructed microstructures are selected to obtain the average F^{avg} for a given porosity. Due to the sufficiently large computational domain we adopted, all of the maximum relative deviations of $D_{O_2,CL}^{eff}$ for the given porosities are within 1%. This is supported by Fathi et al. [55], who conducted a parameter analysis of the domain size on the effective diffusivity and found that there is a small variability for the domain size higher than 0.5 μm. To compute the local Knudsen diffusivity, the pore size diameter at each pore voids throughout the computational domain is required. Lange et al. [56] reported a 13-avearging-length algorithm to compute the pore size distribution, however, the pore size distribution is overestimated as addressed by Zheng and Kim [57]. Following Sabharwal et al. [58], a sphere-fitting algorithm is adopted to account for the local Knudsen resistance in the present work. Fig. 4(b) presents the pore size distributions with porosities of 0.2~0.65. The mean pore diameter decreases from 80.7 to 39.5 nm with porosity. The minimum pore size that can be characterized is 2.5 nm due to the mesh resolution. As seen in Fig. 4(a), our results match well with Zheng and Kim [57], Shin et al. [59], Sabharwal et al. [58], and Fathi et al. [55]. Compared with the data predicted by Lange et al. [56], our data is relatively small due to the difference in the algorithm to obtain the PSD. Compared with the data of Yu et al. [60], our data is relatively high possibly due to the difference in the CL microstructures, which is also addressed in Sabharwal et al. [58].

Fig. 4 Determination of the effective diffusivity in CL, (a) comparison of average formation factor F^{avg} for the stochastic reconstruction methods with existing studies [55-60]; (b) pore size distributions for different porosities

4.2 Validation of the local transport resistances

As addressed before, the reduction of the oxygen permeability coefficient in ionomer thin-film, the limited adsorption rate at Pt surface k_{ads}, or a combination of them, account for the local transport resistance. Since the experimental quantifications of the interfacial resistance are sparse as the ionomer thickness is limited to nanoscale, three sets of the model

parameters are thus selected based on the parameter sensitivity analyses performed later in this section. For the model parameters presented in Fig. 4, k_{ads}^{-1}=0 s□m^{-1} means there is no interfacial transport resistance and ψ_0□ψ_{O2}^{-1}=1 means the adopted permeability coefficient in the simulation is the same as the bulk one.

As shown in Fig. 5, the simulated R_{CL} for cases 1 to 5 with three sets of model parameters are in high accordance with the experimental data carried out by Grezler et al. [11]. R_{CL} presents a roughly linear relationship with the inverse of f_{Pt} and increases greatly with decreasing L_{Pt}. The fit slope k of the experimental data is 1282 s□m^{-1}. This suggests that a combination of the model parameters such as ψ_{O2} and k_{ads} can well reproduce R_{CL} for different L_{Pt} with the same structural parameters (e.g., ω and γ). As the simulated three curves with different model parameters are quite similar, only the curve with the model parameters of k_{ads}^{-1} = 60 s□m^{-1} and ψ_0□ψ_{O2}^{-1}=5 is selected for the following analyses. The calculated $R_{O_2}^{Pt}$ for cases 1 to 5 based on Eq. (2) are 1237, 1283, 1286, 1306, and 1433 s□m^{-1}, respectively. Therefore, approximately a 16% increase of $R_{O_2}^{Pt}$ is observed for y_{bare} decreasing from 0.93 to 0 with constant ω and γ. As addressed by Owejan et al. [12] and Mu et al. [15], f_{Pt} cannot be served as the only indicator to characterize the performance loss; additional geometric considerations accounting for the ionomer surface area relative to the Pt particles are required. The ionomer roughness factor f_{ion}, defined as the total ionomer/pore interfaces normalized by A_{CL}, can be regarded as the surface area for oxygen permeating from pores to ionomer. As f_{ion}□f_{Pt}^{-1} decreases, a relatively smaller effective surface area for the permeation of oxygen is expected, thereby leading to a higher $R_{O_2}^{Pt}$.

Based on Eq. (5), the fit slope k for the simulated data by fixing the intercept of 46 s□m^{-1} (i.e. $R_{O2,\ CH+GDL}$) is around 1292 s□m^{-1}, resulting in a maximum relative deviation around 11% between the linear fitted $R_{O_2}^{Pt}$ and that calculated of case 5 using Eq. (2). The difference is attributed to the fact that l/ψ is far higher than 0. Take case 1 as an example, by substituting the values l=13.6μm, $D_{O_2,CL}^{eff}$=2.5963×10^{-6}m^2□s^{-1} (see Fig. 4(a)), f_{Pt}=14.83 m$_{Pt}^2$□m$_{MEA}^2$ (see Fig. 2(f) or Fig. 3), and $R_{O_2}^{Pt}$=1237 s□m^{-1} in $\psi = \sqrt{D_{O_2,CL}^{eff} l R_{O_2}^{Pt} / f_{Pt}}$, one can find that l/ψ is

around 0.25. This indicates that errors may be introduced to estimate $R_{O_2}^{Pt}$ to some extent by the linear fitting method. Nevertheless, the fit slope k can give a general accurate relationship between R_{CL} and f_{Pt}, and therefore it is adopted in the following parameter analyses.

Fig. 5 Comparison of the total transport resistance versus f_{Pt}, and R_{CL} versus L_{Pt} between the experimental data [11] and the numerical predicted ones with three sets of model parameters

To examine the impact of the adsorption rate k_{ads} and the ratio of the permeation coefficients $\psi_0 \square \psi_{O2}^{-1}$ on k, parameter analyses are performed by altering $\psi_0 \square \psi_{O2}^{-1}$ from 1 to 12 and k_{ads}^{-1} from 0 to 150 s$\square$m^{-1}. As depicted in Fig. 6, the fit slope k increases with k_{ads}^{-1} and $\psi_0 \square \psi_{O2}^{-1}$. For the model parameters of k_{ads}^{-1}=0 s$\square$m^{-1} and $\psi_0 \square \psi_{O2}^{-1}$ =1, the fit slope is around 150 s$\square$m^{-1}, which is about one order-of-magnitude lower than the experimental one. This result agrees well with the existing studies [2, 3, 10]. The contour line with the slope k of 1292 s$\square$m^{-1} exactly fits the experimental data of Grezler et al. [11]. Different sets of the model parameters at this line represent different origins of the additional transport losses. For example, the additional transport resistance is mainly attributed to the adsorption resistance if the model parameters of k_{ads}^{-1}=122 s$\square$m^{-1} and $\psi_0 \square \psi_{O2}^{-1}$ =1 are selected, or the reduction of the transport properties if those of k_{ads}^{-1}=0 s$\square$m^{-1} and $\psi_0 \square \psi_{O2}^{-1}$ =10.5 are selected. Therefore, further validation work is highly needed to demonstrate the origins of the local transport resistance, namely, different experiments with varying ionomers, CL structure, loadings, operating conditions, etc.

Fig. 6 Parameter sensitivity analyses of the adsorption rate k_{ads} and the ratio $\psi_0 \square \psi_{O2}^{-1}$ on the fit slope k

Simulation work on cases 6 to 10 is conducted based on the experimental work performed by Owejan et al. [12]. The operating conditions and the structural parameters of CLs are the same with their experiment. L_{Pt} is held as a constant at 0.025 mg$\square$cm^{-2} by diluting the bare carbons in Pt/C mixtures with different ω. Illustration of the Pt distribution is provided in Fig. 2(d). As depicted in Fig. 7, the result predicted with the model parameters of k_{ads}^{-1}=60 s$\square$m^{-1} and $\psi_0 \square \psi_{O2}^{-1}$ =5 matches well with the experimental data. The simulated R_{CL} for the studied model parameters increases with y_{bare} or ω. This suggests that the dispersion of

Pt particles in carbon particles should be as uniform as possible to achieve better cell performance. The Pt particles dispersed on the supporting primary carbons increase with ω, resulting in shorter transport pathways for oxygen permeating from pores to the active Pt/ionomer surface [48]. However, the effective ionomer roughness factor f_{ion} is highly reduced with the decreasing Pt/C mixture particles, and therefore the oxygen flux relative to discrete Pt particles decreases due to lower $f_{ion}\square f_{Pt}^{-1}$, which also agrees with our previous work on modeling the hydrogen transport resistance [15]. One can also find that R_{CL} changes the most if the model parameters of k_{ads}^{-1}=0 s$\square$m^{-1} and $\psi_0\square\psi_{O2}^{-1}$ =10.2 are adopted. This is reasonable as $R_{O_2}^{Pt}$ predicted with the above model parameters is completely attributed to the oxygen permeation through the ionomer thin-film. Based on the above analyses in terms of different structural parameters and the operation conditions, it is convincible to choose the parameters of k_{ads}^{-1}=60 s$\square$m^{-1} and $\psi_0\square\psi_{O2}^{-1}$ =5 for the following studies. This also indicates that the origin of the additional local transport resistance is attributed to the combined effects of the reduced transport properties and the adsorption resistance at the Pt/ionomer surfaces. The reduction of the transport properties is also supported by Mashio et al. [32], who found that the gas permeability of the ionomer thin-film was 5 to 25% of its bulk material.

Fig. 7 Comparison of the impact of the carbon dilution on R_{CL} between the experimental data [12] and the simulated ones with three sets of model parameters

4.3 Impact of the relative humidity

Typically, the cell RH is kept high enough to avoid the ohmic resistance limiting and a resulting non-uniform current distribution. However, liquid water may accumulate and lead to dramatic changes to R_{Pore} by blocking pore voids and R_{Film} by developing an additional liquid film. Regardless of the effect of the possible liquid water, the variation of the oxygen permeability ψ_{O2} with RH also impacts the local transport resistance. In essence, ψ_{O2} is exponentially proportional to RH as the increase in the diffusion coefficient $D_{ion,O2}$ is more significant than the decrease in solubility H [34].

To explore the impact of RH on $R_{O_2}^{Pt}$, three different cases with L_{Pt} of 0.03, 0.1 and 0.4 mg$\square$cm^{-2} (corresponding to cases 1, 3, and 5 in Table 1) are selected. The oxygen molar

fraction x_{O2} is given as 3%. RH varies from 20 to 100% while keeping the remaining operation conditions the same. As depicted in Fig. 8(a), a slight decrease followed by a sudden increase of $R_{O_2}^{Pt}$ with RH can be observed. Qualitatively, a similar trend can be found in the experimental works of Nonoyama et al. [28], and Iden et al. [30]. The simulated saturations s_{CL} for different L_{Pt} are also presented in this figure, indicating that the increase of $R_{O_2}^{Pt}$ with higher RH is mainly attributed to the presence of the liquid water. Kudo et al. [14], Schuler et al. [22], Shen et al. [23] and Conde et al. [61] also reported a decreasing local transport resistance with RH up to a maximum tested RH of 90%. It should be noted that $D_{O_2,CL}^{eff}$ is corrected here by multiplying 1-s_{CL} to include the effect of the liquid saturation on tortuosity for the determination of $R_{O_2}^{Pt}$. For RH increasing from 20 to 60%, $R_{O_2}^{Pt}$ values decrease 288.44, 344.58, and 408.70 s□m^{-1} for L_{Pt} of 0.03, 0.1, and 0.4 mg□cm^{-2}, respectively. As no liquid water exists with RH up to 60%, the drops of $R_{O_2}^{Pt}$ is entirely attributed to the bulk diffusion in the ionomer thin-film. The limiting current density for L_{Pt} of 0.4 mg□cm^{-2} is the highest, $R_{O_2}^{Pt}$ thereby reduces the most owing to the most humid ionomer. Approximately a drop by 24% of $R_{O_2}^{Pt}$ for RH increasing from 20 to 60% is observed for L_{Pt} of 0.4 mg□cm^{-2}. As RH increases, the water vapor in the pore voids condenses and develops additional liquid film, resulting in higher $R_{O_2}^{Pt}$. It can be found that the liquid saturation increases slightly with RH, which is due to the fact that the oxygen partial pressure decreases with RH. Specifically, the oxygen partial pressure is about 19% larger at 20% RH compared with 100% RH for the same total pressure. The relatively lower oxygen concentration may result in a lower current density and therefore a smaller water production.

Fig. 8 (b) shows the detailed limiting current density i_{lim} and the transport resistance R_{CL} versus RH. Similar with $R_{O_2}^{Pt}$, R_{CL} decreases with RH first and then increases slightly. Note that R_{CL} varies the most for L_{Pt} of 0.03 mg□cm^{-2} owing to its smallest f_{Pt}. i_{lim} is highly related to the oxygen partial pressure and R_{CL}, and a tradeoff between the variations of the oxygen partial pressure and R_{CL} versus RH results in a complicated relationship between i_{lim} and RH for different L_{Pt}. For example, i_{lim} for L_{Pt} of 0.03 mg□cm^{-2} increases firstly owing to the

reduced R_{Film}, and then decreases owing to the decreased oxygen partial pressure and the increased liquid saturation. Combined with the analyses above, it can be inferred that the water transport process in CL should be considered simultaneously to analyze $R_{\mathrm{O_2}}^{\mathrm{Pt}}$.

At RH=80%, water vapor throughout CLs is oversaturated for L_{Pt} of 0.1 and 0.4 mg□cm^{-2}. Fig. 8 (c) illustrates the liquid-water distributions in CLs for different L_{Pt} at RH=100%. In this figure, the liquid water is colored with cyan and the solid components of CL (carbon, platinum and ionomer) are colored with black. As described in Section 3.2, liquid water is randomly attached on the solid components to form water films. It is reasonable that the liquid saturation s_{CL} increases with L_{Pt} from 0.101 to 0.127 at RH=100%. An increase by 12% of $R_{\mathrm{O_2}}^{\mathrm{Pt}}$ for RH increasing from 60 to 100% is found for L_{Pt} of 0.4 mg□cm^{-2}. Reasons can be explained as follows. The volume fraction of liquid water at RH=100% is around 0.0826 (a product of s_{CL} and porosity ε), which is approximately 51% of the volume fraction of ionomer thin-film (0.1628). Meanwhile, the permeation coefficient of oxygen in liquid water is approximately 11.9 times higher than that in the ionomer thin-film. In addition, only the liquid water film coated on non-diluted carbon mixtures contributes to the local transport resistance. The above three factors make the hindering effect of liquid water on the local transport resistance of oxygen insignificant. Notably, the isothermal assumption made in this work may overestimate liquid condensation as the local heat generation (and hence evaporation) increases as loading decreases. Therefore, additional transport resistance originated from the liquid water may be overestimated. Finally, it should be noted that we assume the same underlying microstructure for the various studies. This assumption is somewhat at odds with recent results that demonstrate that CL formation is also a function of the processing and base material interactions, which could change due to solvent, ionomer ratio, etc. [62]. In our simulation, we do not consider this due to a lack of relevant experimental data.

Based on the above analyses, it is suggested that a smaller oxygen concentration and lower L_{Pt} are favored to avoid the accumulation of liquid water. RH should be kept under 80%. As the local transport processes of oxygen and water are closely coupled, one cannot ignore the influence of the water transport to clarify $R_{\mathrm{O_2}}^{\mathrm{Pt}}$. Apart from RH, the molar fraction of

oxygen x_{O2} is also essential as i_{lim} presents a positive relationship with x_{O2}. The impact of x_{O2} on the transport resistances of oxygen is thereby presented below to further illustrate the deconvolution of the transport resistances.

Fig. 8 Impacts of the relative humidity RH on the transport process in CL for three different L_{Pt}, (a) $R_{O_2}^{Pt}$ versus RH; (b) R_{CL} and i_{lim} versus RH; (c) snapshots of the liquid distributions for x ranging from 5.5 to 6.5 μm

4.4 Impact of the oxygen molar concentration

To avoid the condensation of liquid water, the maximum x_{O2} at a given RH is typically determined by gradually increasing x_{O2} and examining the oxygen transport resistance until a sufficiently large variation is observed [34]. In the present work, we have examined the impact of x_{O2} on the transport resistances of oxygen. Three different cases with L_{Pt} of 0.03, 0.1 and 0.4 mg□cm^{-2} (corresponding to cases 1, 3, and 5 in Table 1) are selected. RH is specified as 80%, and x_{O2} varies from 1 to 7% while maintaining the rest parameters the same.

As illustrated in Fig. 9 (a), $R_{O_2}^{Pt}$ value remains to be a constant for L_{Pt} of 0.03 mg□cm^{-2} with x_{O2} up to 3%, and only a 0.3% drop is observed for x_{O2} ranging from 1% to 3% due to a slightly humidified ionomer thin-film caused by the water production in CL. However, the respective increases by 4.1% and 9.7% of $R_{O_2}^{Pt}$ for x_{O2} increasing from 1% to 3% are witnessed for L_{Pt} of 0.1 and 0.4 mg□cm^{-2} owing to the presence of liquid water. As x_{O2} and L_{Pt} increase, the liquid water appears earlier due to a higher limiting current density. Qualitatively our result agrees well with the experimental data provided by Oh et al. [34], who suggested that the oxygen should be supplied at a concentration less than 4% and a RH below 90%. Shen et al. [23] also reported a slight variation of $R_{O_2}^{Pt}$ when x_{O2} ranges from 1% to 2%, and an 45% increase $R_{O_2}^{Pt}$ for x_{O2} ranging from 1% to 8%. Due to a higher RH we adopted, the simulated liquid saturation for L_{Pt} of 0.4 mg□cm^{-2} increases from 0.11 to 0.155 for x_{O2} varying from 3% to 7%, and correspondingly $R_{O_2}^{Pt}$ increases from 1434.3 to 1494.6 s□m^{-1}. The slightly changed s_{CL}, together with the high permeation coefficient of oxygen in the liquid water, accounts for the insignificant variation of $R_{O_2}^{Pt}$ versus x_{O2}. In the present study, an

increase by 14% of $R_{O_2}^{Pt}$ for x_{O2} ranging from 1% to 7% is found. Based on the above analyses, both L_{Pt} and x_{O2} should be kept as low as possible to avoid the occurrence of liquid condensation.

Fig. 9 (b) presents the impacts of x_{O2} on the transport resistances contributed by ionomer R_{Film} and pores R_{Pore}. Definitions on these two transport resistances are given in Section 2.1. For L_{Pt} of 0.4 mg□cm^{-2}, R_{Pore} increases from 1.5 to 1.7 s□m^{-1} due to the decreased effective diffusion coefficient and the increased local transport resistance; while R_{Film} increases from 5.9 to 6.8 s□m^{-1} due to the presence of liquid water. For L_{Pt} of 0.03 mg□cm^{-2}, R_{Pore} increases from 1.5 to 1.7 s□m^{-1}, and R_{Film} increases from 75.2 to 77.5 s□m^{-1}. It can be found that R_{Film} is more sensitive to the liquid saturation than R_{Pore}, and the contribution of R_{Pore} to the total transport resistance can be ignored for low-loaded CL. Fig. 9 (c) illustrates the snapshots of the liquid distributions of L_{Pt} of 0.1 mg□cm^{-2} for different x_{O2}. The liquid nodes colored with cyan increase with x_{O2}, making the oxygen permeating from pores to Pt/ionomer difficult. Therefore, it can be found that the operation conditions are critical to clarify $R_{O_2}^{Pt}$ originated from the structure itself. To maintain an under-saturated condition inside the cell, x_{O2} of 1% and RH of 62% are selected to investigate the impacts of the structural parameters on the transport resistances.

Fig. 9 Impacts of the oxygen molar fractions x_{O2} on the transport process in the CL for three different L_{Pt}, (a) $R_{O_2}^{Pt}$ versus x_{O2}; (b) transport resistances versus x_{O2}; (c) snapshots of the liquid distributions for x ranging from 5.5 to 6.5 μm

4.5 Impact of the structural parameters

As the CL design depends on several fundamental structural parameters, i.e., Pt/C ratio ω and I/C ratio γ, a comprehensive understanding of these structural parameters on $R_{O_2}^{Pt}$ is essential. To explore the impact of I/C ratio γ on the transport resistances in CL, the structural parameters of l=12 μm, L_{Pt} = 0.2 mg□cm^{-2}, ω = 51.8%, and y_{bare}=0.5 are held as constant, and only γ changes from 0.6 to 1.3. The corresponding ε and the simulated f_{Pt} with the reconstruction method are presented in Fig. 10 (a). It is understandable that f_{Pt} increases with γ as more Pt surfaces become active for electrochemical reactions. Possibly due to the

sufficiently higher ω we adopted, only a ~6% increase is observed. With more ionomer added in CL, ε decreases accordingly. As seen in this figure, $R_{O_2}^{Pt}$ increases monotonically with γ due to a relatively thick ionomer thin-film coated on the reaction sites. The volume fraction distribution of the ionomer thickness for γ =0.6 and 1.3 are depicted in SI. The mean thicknesses of the ionomer thin-film for γ =0.6 and 1.3 are 6.5 and 15.6 nm, respectively. This explains a higher local transport resistance $R_{O_2}^{Pt}$ with γ. A 42% increase of $R_{O_2}^{Pt}$ is observed for γ ranging from 0.6 to 1.3. By using a hydrogen-limiting-current strategy, a 64% increase of the local transport resistance of hydrogen for γ ranging from 0.6 to 1.1 was experimentally observed by Schuler et al. [22]. We also numerically reported a 60% increase of the local transport resistance of hydrogen for γ ranging from 0.6 to 1.1 [15].

Mashio et al. [63] attributed this phenomenon to the difference in porosity as the effective Knudsen diffusion coefficient is affected by the porosity. Therefore, the transport resistances of ionomer and pores versus γ are also plotted in this figure. It can be found that R_{Pore} increases from 2.0 to 5.0 s□m^{-1} and R_{Film} increases from 8.2 to 11.0 s□m^{-1}. Therefore, R_{Pore} occupies 20% to 31% of the total transport resistance for γ ranging from 0.6 to 1.3. It indicates that both the increased ionomer thickness and the decreased Knudsen diffusion coefficient account for the increased transport resistance in CL with high γ. As expected, $R_{O_2}^{Pt}$ increases linearly with γ. However, our recent experimental data suggested that $R_{O_2}^{Pt}$ increases more at higher γ because of more secondary-pore filling and possibly a different structure of the CL due possibly to changing interactions of the ionomer and catalysts. In the present study, the porosity of the CL only changes from 0.417 to 0.584 for γ ranging from 1.3 to 0.6, therefore a little bit of the secondary pores may be filled due to the relatively high porosity.

Fig. 10 (b) presents the impact of Pt/C ratio ω on the transport resistances of CL. The structural parameters of CL are specified as l=12 μm, ε=0.5, γ=0.95, and y_{bare}=0.5. Detailed ω and the corresponding f_{Pt} are listed in the figure. Accordingly, L_{Pt} can be easily calculated as a_{ECSA} is fitted as 67.11 m_{Pt}^2□g_{Pt}^{-1}. Note that Pt/C ratio ω represents the catalyst mass fraction of the undiluted Pt/C mixture. Although the ionomer thin-film may become more humidified

with high L_{Pt} and hence lower the local transport resistance. However, the water content changes slightly from 4.79 to 5.21 due to the low i_{lim}. The ionomer roughness factor f_{ion} for different ω changes slightly from 534.7 to 523.4 $m_{ion}^2 \cdot m_{MEA}^{-2}$, while f_{Pt} changes from 20.6 to 166.5 $m_{Pt}^2 \cdot m_{MEA}^{-2}$. This results in a decreasing effective surface area of ionomer relative to the reactive surfaces $f_{ion} \cdot f_{Pt}^{-1}$, thereby giving rise to an increasing $R_{O_2}^{Pt}$ with ω. A 49% $R_{O_2}^{Pt}$ increase is observed for L_{Pt} varies from 0.03 to 0.25 $mg \cdot cm^{-2}$. As R_{Film} is inversely proportional to f_{Pt} (i.e. L_{Pt}), it decreases from 44.3 to 8.1 $s \cdot m^{-1}$. A slight change of R_{Pore} due to the impact of $R_{O_2}^{Pt}$ is observed from 3.1 to 2.6 $s \cdot m^{-1}$. R_{Pore} accounts for 6.5% to 24.3% of R_{CL} with ω increasing from 9.8% to 60.9%, respectively. Comparing L_{Pt} of 0.05 $mg \cdot cm^{-2}$ with that of 0.20 $mg \cdot cm^{-2}$, R_{CL} less than triples upon quadrupling L_{Pt}. Therefore, it is economic to design the electrode with lower ω as higher current density can be produced under constant L_{Pt}. This result agrees well with the distribution of the electrochemical reaction rate j shown in Fig. S3 (a).

Fig. 10 Impacts of the structural parameters of CLs on the transport resistances, (a) I/C ratio γ for the structural parameters of l = 12 μm, L_{Pt} = 0.2 $mg \cdot cm^{-2}$, ω = 51.8%, and y_{bare}=0.5; (b) Pt/C ratio ω for the structural parameters of l = 12 μm, ε = 0.5, γ=0.95, and y_{bare}=0.5

5. Conclusion

Oxygen transport resistances in a reconstructed microstructure of a cathode CL were numerically predicted using a mesoscopic method considering the detailed local transport processes of oxygen in pores, ionomer, and liquid water. Characterizations of the reconstructed microstructures in terms of the distributions of the carbon size, ionomer thin-film thickness, and roughness factor were carried out. Limiting current densities for different structural parameters under different operation conditions were obtained and compared against experimental data based on the oxygen-limiting-current method. Local transport resistance and the contribution of pores to R_{CL} were analytically solved after the effective diffusivity of CL was achieved. The main conclusions are as follows.

(1) Oxygen transport resistances in other components of the cell (i.e. CH and GDL) dominate for high L_{Pt}. The oxygen concentration distribution in the pores is relatively uniform,

while that in ionomer varies greatly due to the ionomer distribution and uneven electrochemical reaction rate.

(2) The maximum relative deviation of $R_{O_2}^{Pt}$ predicted with the linear fitting method and the analytical method is around 11%. Parameter analyses, together with the validation work between the simulated data and the existing experimental studies in terms of different RH and structural parameters, suggest that the combination of the reduced permeation coefficient and the adsorption resistance accounts for the origins of the local transport resistance.

(3) A slight decrease followed by an increase of $R_{O_2}^{Pt}$ versus RH can be found, with the increasing trend attributed to the presence of the liquid water. Compared with R_{Pore}, R_{Film} is more sensitive to the liquid saturation. $R_{O_2}^{Pt}$ increases with the oxygen molar fraction and the platinum loading owing to the presence of the liquid water. $R_{O_2}^{Pt}$ increases with I/C ratio γ and the Pt/C ratio ω due to the increased ionomer thickness and the decreased Knudsen diffusion coefficient, and a decreasing ionomer surfaces area for the permeation of oxygen per Pt site, respectively.

Acknowledgements

This work is supported by the National Natural Science Foundation of China (51806170), the National Postdoctoral Program for Innovative Talents (BX201700190) and the National Postdoctoral Program Foundation of China (2017M620450). AZW acknowledges his funding through the Fuel Cell Performance and Durability Consortium (FC-PAD), and Office of Energy Efficiency and Renewable Energy (EERE), of the U.S. Department of Energy under contract number DE-AC02-05CH11231.

References

1. Stephens, I.E.L., J. Rossmeisl, and I. Chorkendorff, *Toward sustainable fuel cells.* Science, 2016. **354**(6318): p. 1378-1379.
2. Kongkanand, A. and M.F. Mathias, *The Priority and Challenge of High-Power Performance of Low-Platinum Proton-Exchange Membrane Fuel Cells.* J Phys Chem Lett, 2016. **7**(7): p. 1127-37.
3. Banham, D. and S. Ye, *Current Status and Future Development of Catalyst Materials and Catalyst Layers for Proton Exchange Membrane Fuel Cells: An Industrial Perspective.* ACS Energy Letters, 2017. **2**(3): p. 629-638.
4. Yoshida, T. and K. Kojima, *Toyota MIRAI fuel cell vehicle and progress toward a future hydrogen society.* The Electrochemical Society Interface, 2015. **24**(2): p. 45-49.
5. Haug, A., *Novel ionomers and electrode structures for improved PEMFC electrode performance at low PGM loadings*, in *Annual Merit Review and Evaluation Meeting*. 2018, DOE Hydrogen and Fuel Cells Program: Washington, DC.
6. Wang, Y.-J., B. Fang, H. Li, X.T. Bi, and H. Wang, *Progress in modified carbon support materials for Pt and Pt-alloy cathode catalysts in polymer electrolyte membrane fuel cells.* Progress in Materials Science, 2016. **82**: p. 445-498.
7. Bu, L., N. Zhang, S. Guo, X. ZHang, J. Li, J. Yao, and T. Wu, *Biaxially strained PtPb/Pt core/shell nanoplate boosts oxygen reduction catalysis.* Science, 2016. **354**(6318): p. 1410-1414.
8. Li, M., Z. Zhao, T. Cheng, A. Fortunelli, C.-Y. Chen, R. Yu, Q. Zhang, and L. Gu, *Ultrafine jagged platinum nanowires enable ultrahigh mass activity for the oxygen reduction reaction.* Science, 2016. **354**(6318): p. 1414-1419.
9. Sui, S., X. Wang, X. Zhou, Y. Su, S. Riffat, and C.-j. Liu, *A comprehensive review of Pt electrocatalysts for the oxygen reduction reaction: Nanostructure, activity, mechanism and carbon support in PEM fuel cells.* Journal of Materials Chemistry A, 2017. **5**(5): p. 1808-1825.
10. Weber, A.Z. and A. Kusoglu, *Unexplained transport resistances for low-loaded fuel-cell catalyst layers.* J. Mater. Chem. A, 2014. **2**(41): p. 17207-17211.
11. Greszler, T.A., D. Caulk, and P. Sinha, *The impact of platinum loading on oxygen transport resistance.* Journal of The Electrochemical Society, 2012. **159**(12): p. F831-F840.
12. Owejan, J.P., J.E. Owejan, and W. Gu, *Impact of platinum loading and catalyst layer structure on PEMFC performance.* Journal of The Electrochemical Society, 2013. **160**(8): p. F824-F833.
13. Suzuki, T., K. Kudo, and Y. Morimoto, *Model for investigation of oxygen transport limitation in a polymer electrolyte fuel cell.* Journal of Power Sources, 2013. **222**: p. 379-389.
14. Kudo, K., R. Jinnouchi, and Y. Morimoto, *Humidity and Temperature Dependences of Oxygen Transport Resistance of Nafion Thin Film on Platinum Electrode.* Electrochimica Acta, 2016. **209**: p. 682-690.
15. Mu, Y.-T., A.Z. Weber, Z.-L. Gu, and W.-Q. Tao, *Mesoscopic modeling of transport resistances in a polymer-electrolyte fuel-cell catalyst layer: Analysis of hydrogen limiting currents.* Applied Energy, 2019. **255**: p. 113895.
16. Cetinbas, F.C., R.K. Ahluwalia, N. Kariuki, V. De Andrade, D. Fongalland, L. Smith, J. Sharman, P. Ferreira, S. Rasouli, and D.J. Myers, *Hybrid approach combining multiple characterization techniques and simulations for microstructural analysis of proton exchange membrane fuel cell electrodes.* Journal of Power Sources, 2017. **344**: p. 62-73.
17. Chowdhury, A., C.J. Radke, and A.Z. Weber, *Transport Resistances in Fuel-Cell Catalyst Layers.* ECS Transactions, 2017. **80**(8): p. 321-333.
18. Kusoglu, A. and A.Z. Weber, *New Insights into Perfluorinated Sulfonic-Acid Ionomers.* Chem Rev, 2017.

117(3): p. 987-1104.
19. Page, K.A., A. Kusoglu, C.M. Stafford, S. Kim, R.J. Kline, and A.Z. Weber, *Confinement-driven increase in ionomer thin-film modulus.* Nano Lett, 2014. **14**(5): p. 2299-304.
20. Kusoglu, A., T.J. Dursch, and A.Z. Weber, *Nanostructure/Swelling Relationships of Bulk and Thin-Film PFSA Ionomers.* Advanced Functional Materials, 2016. **26**(27): p. 4961-4975.
21. Freiberg, A.T.S., M.C. Tucker, and A.Z. Weber, *Polarization loss correction derived from hydrogen local-resistance measurement in low Pt-loaded polymer-electrolyte fuel cells.* Electrochemistry Communications, 2017. **79**: p. 14-17.
22. Schuler, T., A. Chowdhury, A.T.S. Freiberg, B. Sneed, F.B. Spingler, M.C. Tucker, K.L. More, C.J. Radke, and A.Z. Weber, *Fuel-cell catalyst-layer resistance via hydrogen limiting-current measurements.* Journal of The Electrochemical Society, 2019. **166**(7): p. F3020-F3031.
23. Shen, S., X. Cheng, C. Wang, X. Yan, C. Ke, J. Yin, and J. Zhang, *Exploration of significant influences of the operating conditions on the local O2 transport in proton exchange membrane fuel cells (PEMFCs).* Phys Chem Chem Phys, 2017. **19**(38): p. 26221-26229.
24. Liu, H., W.K. Epting, and S. Litster, *Gas transport resistance in polymer electrolyte thin films on oxygen reduction reaction catalysts.* Langmuir, 2015. **31**(36): p. 9853-9858.
25. Suzuki, T., H. Yamada, K. Tsusaka, and Y. Morimoto, *Modeling of Oxygen Diffusion Resistance in Polymer Electrolyte Fuel Cells in the Intermediate Potential Region.* Journal of The Electrochemical Society, 2018. **165**(3): p. F166-172.
26. Jinnouchi, R., K. Kodama, A. Nagoya, and Y. Morimoto, *Simulated Volcano Plot of Oxygen Reduction Reaction on Stepped Pt Surfaces.* Electrochimica Acta, 2017. **230**: p. 470-478.
27. Mu, Y.-T., P. He, J. Ding, L. Chen, and W.-Q. Tao, *Numerical Study of the Gas Purging Process of a Proton Exchange Membrane Fuel Cell.* Energy Procedia, 2017. **105**: p. 1967-1973.
28. Nonoyama, N., S. Okazaki, A.Z. Weber, Y. Ikogi, and T. Yoshida, *Analysis of oxygen-transport diffusion resistance in proton-exchange-membrane fuel cells.* Journal of The Electrochemical Society, 2011. **158**(4): p. B416-B423.
29. Shukla, S., D. Stanier, M.S. Saha, J. Stumper, and M. Secanell, *Analysis of inkjet printed PEFC electrodes with varying platinum loading.* Journal of The Electrochemical Society, 2016. **163**(7): p. F677-F687.
30. Iden, H., S. Takaichi, Y. Furuya, T. Mashio, Y. Ono, and A. Ohma, *Relationship between gas transport resistance in the catalyst layer and effective surface area of the catalyst.* Journal of Electroanalytical Chemistry, 2013. **694**: p. 37-44.
31. Muzaffar, T., T. Kadyk, and M. Eikerling, *Tipping water balance and the Pt loading effect in polymer electrolyte fuel cells: a model-based analysis.* Sustainable Energy & Fuels, 2018. **2**(6): p. 1189-1196.
32. Mashio, T., H. Iden, A. Ohma, and T. Tokumasu, *Modeling of local gas transport in catalyst layers of PEM fuel cells.* Journal of Electroanalytical Chemistry, 2017. **790**: p. 27-39.
33. Ono, Y., A. Ohma, K. Shinohara, and K. Fushinobu, *Influence of equivalent weight of ionomer on local oxygen transport resistance in cathode catalyst layers.* Journal of The Electrochemical Society, 2013. **160**(8): p. F779-F787.
34. Oh, H., Y.i. Lee, G. Lee, K. Min, and J.S. Yi, *Experimental dissection of oxygen transport resistance in the components of a polymer electrolyte membrane fuel cell.* Journal of Power Sources, 2017. **345**: p. 67-77.
35. Moore, M., P. Wardlaw, P. Dobson, J.J. Boisvert, A. Putz, R.J. Spiteri, and M. Secanell, *Understanding the Effect of Kinetic and Mass Transport Processes in Cathode Agglomerates.* Journal of The Electrochemical Society, 2014. **161**(8): p. E3125-E3137.
36. Secanell, M., A. Putz, S. Shukla, P. Wardlaw, M. Bhaiya, L.M. Pant, and M. Sabharwal, *Mathematical Modeling and Experimental Analysis of Thin, Low-Loading Fuel Cell Electrodes.* ECS Transactions, 2015.

69(17): p. 157-187.
37. Zhou, J., S. Shukla, A. Putz, and M. Secanell, *Analysis of the role of the microporous layer in improving polymer electrolyte fuel cell performance.* Electrochimica Acta, 2018. **268**: p. 366-382.
38. Hao, L., K. Moriyama, W. Gu, and C.-Y. Wang, *Modeling and Experimental Validation of Pt Loading and Electrode Composition Effects in PEM Fuel Cells.* Journal of The Electrochemical Society, 2015. **162**(8): p. F854-F867.
39. Darling, R., *A Comparison of Models for Transport Resistance in Fuel-Cell Catalyst Layers.* Journal of The Electrochemical Society, 2018. **165**(16): p. F1331-F1339.
40. Zhang, X. and Y. Gao, *Impact of liquid water on oxygen reaction in cathode catalyst layer of proton exchange membrane fuel cell: A simple and physically sound model.* Journal of Power Sources, 2016. **318**: p. 251-263.
41. Sabharwal, M., L.M. Pant, A. Putz, D. Susac, J. Jankovic, and M. Secanell, *Analysis of catalyst layer microstructures: from imaging to performance.* Fuel Cells, 2016. **16**(6): p. 734-753.
42. Cetinbas, F.C., X. Wang, R.K. Ahluwalia, N.N. Kariuki, R. Winarski, Z. Yang, J. Sharman, and D.J. Myers, *Microstructural Analysis and Transport Resistances of Low-Platinum-Loaded PEFC Electrodes.* Journal of The Electrochemical Society, 2017. **164**(14): p. F1595-1607.
43. Hou, Y., H. Deng, F. Pan, W. Chen, Q. Du, and K. Jiao, *Pore-scale investigation of catalyst layer ingredient and structure effect in proton exchange membrane fuel cell.* Applied Energy, 2019. **253**: p. 113561.
44. Zenyuk, I.V., P.K. Das, and A.Z. Weber, *Understanding Impacts of Catalyst-Layer Thickness on Fuel-Cell Performance via Mathematical Modeling.* Journal of The Electrochemical Society, 2016. **163**(7): p. F691-F703.
45. Zhang, J., W. Yang, L. Xu, and Y. Wang, *Simulation of the catalyst layer in PEMFC based on a novel two-phase lattice model.* Electrochimica Acta, 2011. **56**(20): p. 6912-6918.
46. Wang, G., P.P. Mukherjee, and C.-Y. Wang, *Direct numerical simulation (DNS) modeling of PEFC electrodes.* Electrochimica Acta, 2006. **51**(15): p. 3151-3160.
47. Guo, Y., J. He, T. Wang, H. Xue, Y. Hu, G. Li, J. Tang, and X. Sun, *Enhanced electrocatalytic activity of platinum supported on nitrogen modified ordered mesoporous carbon.* Journal of Power Sources, 2011. **196**(22): p. 9299-9307.
48. Yoon, W. and A.Z. Weber, *Modeling Low-Platinum-Loading Effects in Fuel-Cell Catalyst Layers.* Journal of The Electrochemical Society, 2011. **158**(8): p. B1007-B1018.
49. Mu, Y.-T., P. He, J. Ding, and W.-Q. Tao, *Modeling of the operation conditions on the gas purging performance of polymer electrolyte membrane fuel cells.* International Journal of Hydrogen Energy, 2017. **42**(16): p. 11788-11802.
50. Perry, R.B. and D.W. Green, *Perry's Chemical Engineers' Handbook*. 1999, New York: McGraw-Hill.
51. Motupally, S., A.J. Becker, and J.W. Weidner, *Diffusion of water in Nafion 115 membranes.* Journal of The Electrochemical Society, 2000. **147**(9): p. 3171-3177.
52. Weber, A.Z., R.L. Borup, R.M. Darling, P.K. Das, T.J. Dursch, W. Gu, D. Harvey, A. Kusoglu, S. Litster, M.M. Mench, R. Mukundan, J.P. Owejan, J.G. Pharoah, M. Secanell, and I.V. Zenyuk, *A Critical Review of Modeling Transport Phenomena in Polymer-Electrolyte Fuel Cells.* Journal of The Electrochemical Society, 2014. **161**(12): p. F1254-1299.
53. Xie, B., G. Zhang, J. Xuan, and K. Jiao, *Three-dimensional multi-phase model of PEM fuel cell coupled with improved agglomerate sub-model of catalyst layer.* Energy Conversion and Management, 2019. **199**: p. 112051.
54. Mu, Y.-T., Z.-L. Gu, P. He, and W.-Q. Tao, *Lattice Boltzmann method for conjugated heat and mass transfer with general interfacial conditions.* Physical Review E, 2018. **98**(4).
55. Fathi, H., A. Raoof, S. Mansouri, and M.T. van Genuchten, *Effects of porosity and water saturation on the*

effective diffusivity of a cathode catalyst layer. Journal of The Electrochemical Society, 2017. **164**(4): p. F298-F305.

56. Lange, K.J., P.-C. Sui, and N. Djilali, *Pore Scale Simulation of Transport and Electrochemical Reactions in Reconstructed PEMFC Catalyst Layers.* Journal of The Electrochemical Society, 2010. **157**(10): p. B1434.

57. Zheng, W. and S.H. Kim, *The Effects of Catalyst Layer Microstructure and Water Saturation on the Effective Diffusivity in PEMFC.* Journal of The Electrochemical Society, 2018. **165**(7): p. F468-F478.

58. Sabharwal, M., L.M. Pant, N. Patel, and M. Secanell, *Computational Analysis of Gas Transport in Fuel Cell Catalyst Layer under Dry and Partially Saturated Conditions.* Journal of The Electrochemical Society, 2019. **166**(7): p. F3065-F3080.

59. Shin, S., A.-R. Kim, and S. Um, *Computational prediction of nanoscale transport characteristics and catalyst utilization in fuel cell catalyst layers by the lattice Boltzmann method.* Electrochimica Acta, 2018. **275**: p. 87-99.

60. Yu, Z., R.N. Carter, and J. Zhang, *Measurements of Pore Size Distribution, Porosity, Effective Oxygen Diffusivity, and Tortuosity of PEM Fuel Cell Electrodes.* Fuel Cells, 2012. **12**(4): p. 557-565.

61. Conde, J.J., M.A. Folgado, P. Ferreira-Aparicio, A.M. Chaparro, A. Chowdhury, A. Kusoglu, D. Cullen, and A.Z. Weber, *Mass-transport properties of electrosprayed Pt/C catalyst layers for polymer-electrolyte fuel cells.* Journal of Power Sources, 2019. **427**: p. 250-259.

62. Van Cleve, T., S. Khandavalli, A. Chowdhury, S. Medina, S. Pylypenko, M. Wang, K.L. More, N. Kariuki, D.J. Myers, A.Z. Weber, S.A. Mauger, M. Ulsh, and K.C. Neyerlin, *Dictating Pt-Based Electrocatalyst Performance in Polymer Electrolyte Fuel Cells, from Formulation to Application.* ACS Appl Mater Interfaces, 2019. **11**(50): p. 46953-46964.

63. Mashio, T., A. Ohma, S. Yamamoto, and K. Shinohara, *Analysis of Reactant Gas Transport in a Catalyst Layer.* ECS Transactions, 2007. **11**(1): p. 529-540.

Figure Captions

Fig. 1 Schematic illustration of the oxygen transport process in the CL porous structure, (a) oxygen transport in voids; (b) local transport resistances of oxygen in ionomer thin-film; (c) oxygen permeation in ionomer thin-film

Fig. 2 Characterization of the reconstructed CL microstructures, (a) CL morphology of case 3 (void: white, carbon: black, platinum: red; ionomer: cyan); (b) locations of Pt particles for different L_{Pt} of cases 3 and 5; (c) comparison of the distributions of carbon particle size and ionomer thin-film thickness between the simulated and experimental data [16] of case 3; (d) locations of Pt particles for different y_{bare} of cases 6 and 10; (e) normalized face-average fractions of the components along the thickness direction of case 3; (f) comparison of f_{Pt} between the simulated cases and experimental data [11, 12]

Fig. 3 Polarization curves of CLs with different L_{Pt}

Fig. 4 Determination of the effective diffusivity in CL, (a) comparison of average formation factor F^{avg} for the stochastic reconstruction methods with existing studies [55-60]; (b) pore size distributions for different porosities

Fig. 5 Comparison of the total transport resistance versus f_{Pt}, and R_{CL} versus L_{Pt} between the experimental data [11] and the numerical predicted ones with three sets of model parameters

Fig. 6 Parameter sensitivity analyses of the adsorption rate k_{ads} and the ratio $\psi_0 \cdot \psi_{O2}^{-1}$ on the slope k

Fig. 7 Comparison of the impact of the carbon dilution on RCL between the experimental data [12] and the simulated ones with three sets of model parameters

Fig. 8 Impacts of the relative humidity RH on the transport process in the CL for three

different L_{Pt}, (a) $R_{O_2}^{Pt}$ versus RH; (b) R_{CL} and i_{lim} versus RH; (c) snapshots of the liquid distributions for x ranging from 5.5 to 6.5 μm

Fig. 9 Impacts of the oxygen molar fractions x_{O2} on the transport process in CL for three different L_{Pt}, (a) $R_{O_2}^{Pt}$ versus x_{O2}; (b) transport resistances versus x_{O2}; (c) snapshots of the liquid distributions for x ranging from 5.5 to 6.5 μm

Fig. 10 Impacts of the structural parameters of CLs on the transport resistances, (a) I/C ratio γ for the structural parameters of l = 12 μm, L_{Pt} = 0.2 mg·cm^{-2}, ω = 51.8% , and y_{bare}=0.5; (b) Pt/C ratio ω for the structural parameters of l = 12 μm, $\sum$= 0.5, γ=0.95, and y_{bare}=0.5

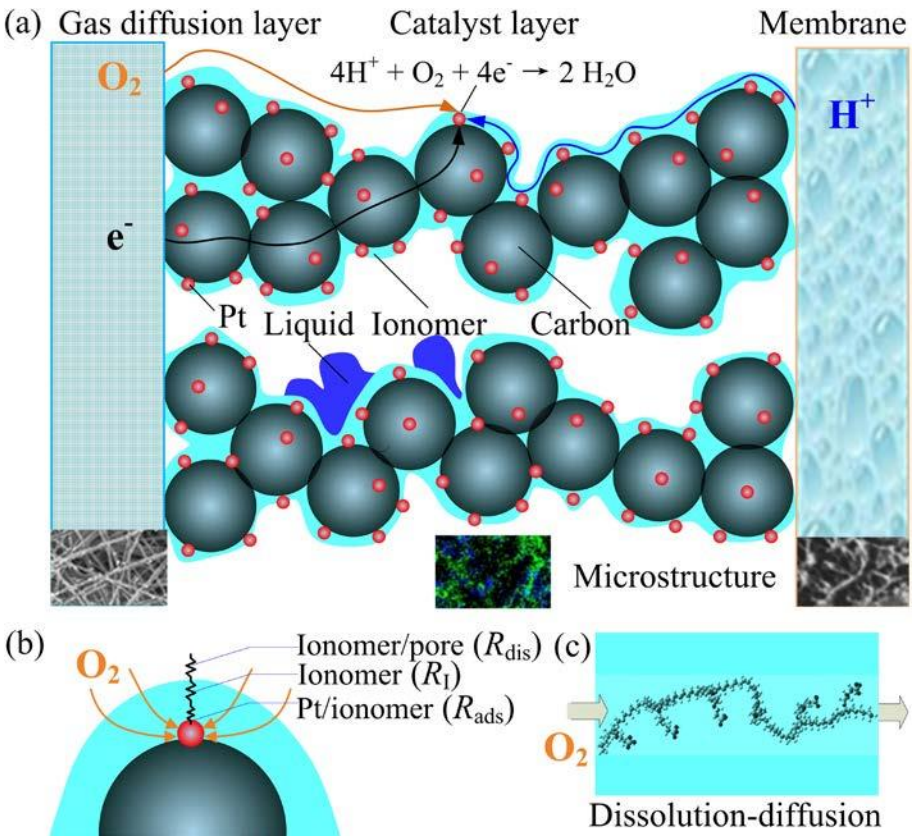

Fig. 1 Schematic illustration of the oxygen transport process in the CL porous structure, (a) oxygen transport in voids; (b) local transport resistances of oxygen in ionomer thin-film; (c) oxygen permeation in ionomer thin-film

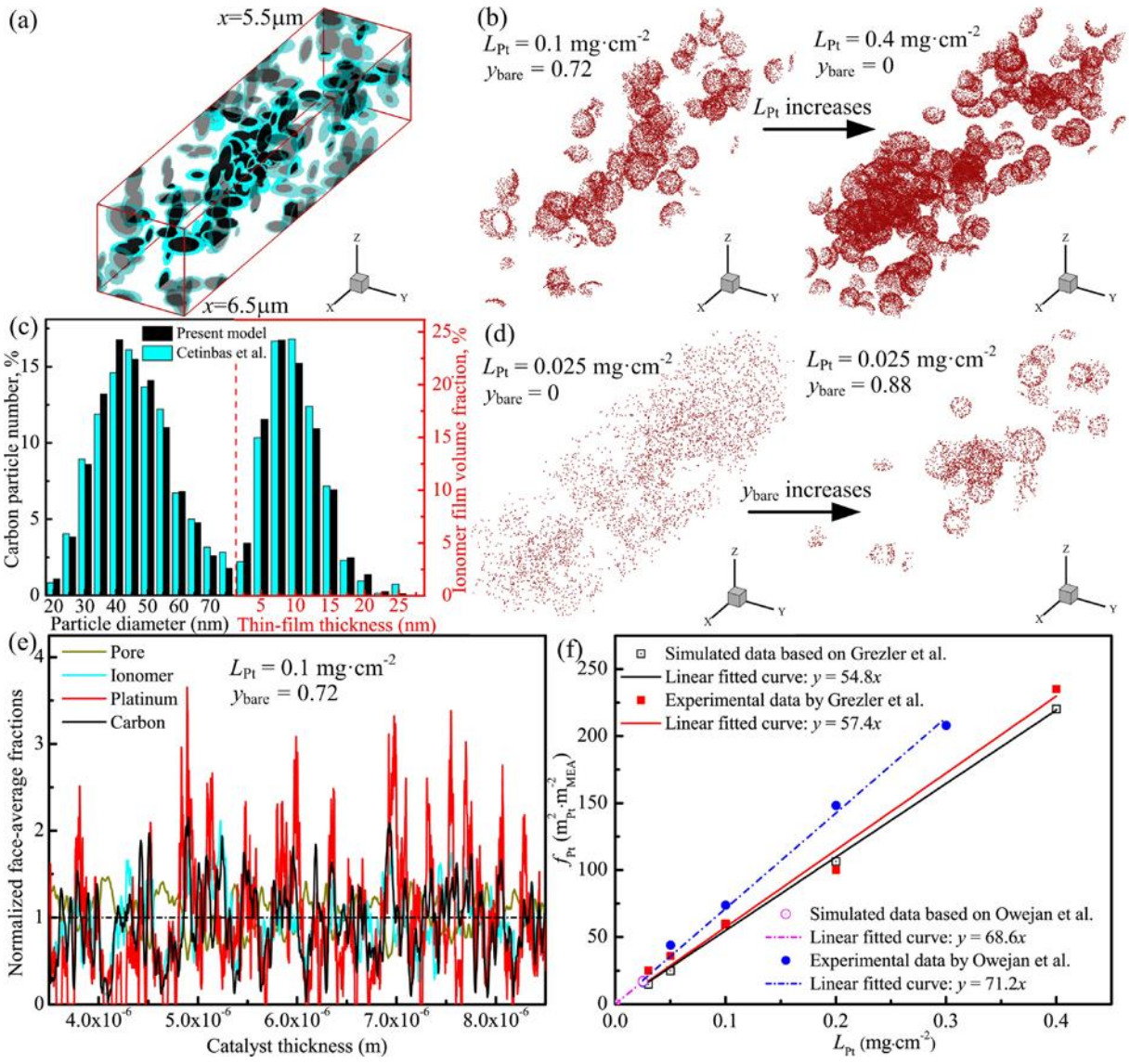

Fig. 2 Characterization of the reconstructed CL microstructures, (a) CL morphology of case 3 (void: white, carbon: black, platinum: red; ionomer: cyan); (b) locations of Pt particles for different L_{Pt} of cases 3 and 5; (c) comparison of the distributions of carbon particle size and ionomer thin-film thickness between the simulated and experimental data [16] of case 3; (d) locations of Pt particles for different y_{bare} of cases 6 and 10; (e) normalized face-average fractions of the components along the thickness direction of case 3; (f) comparison of f_{Pt} between the simulated cases and experimental data [11, 12]

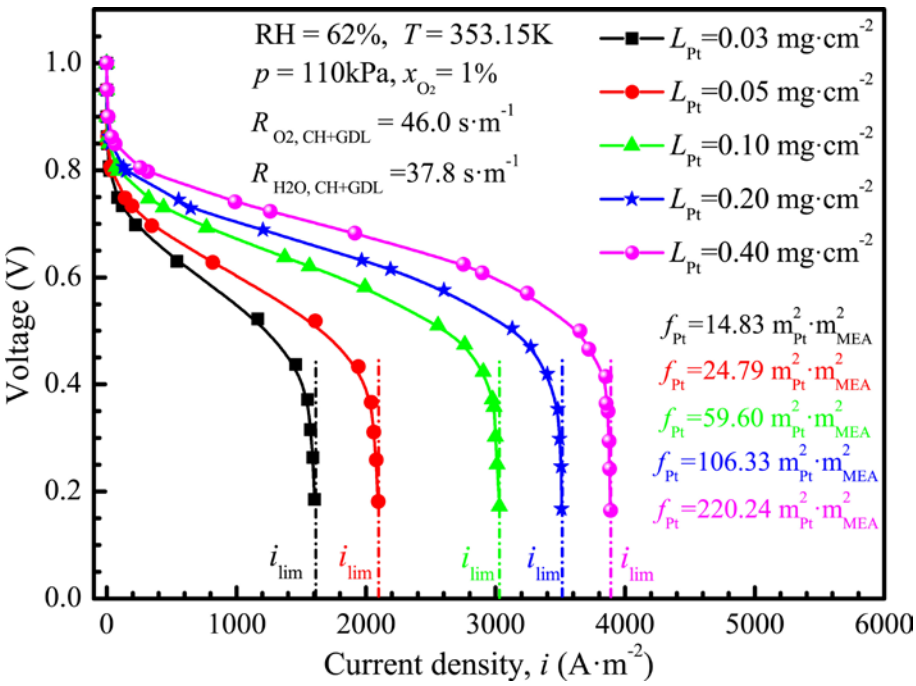

Fig. 3 Polarization curves of CLs with different L_{Pt}

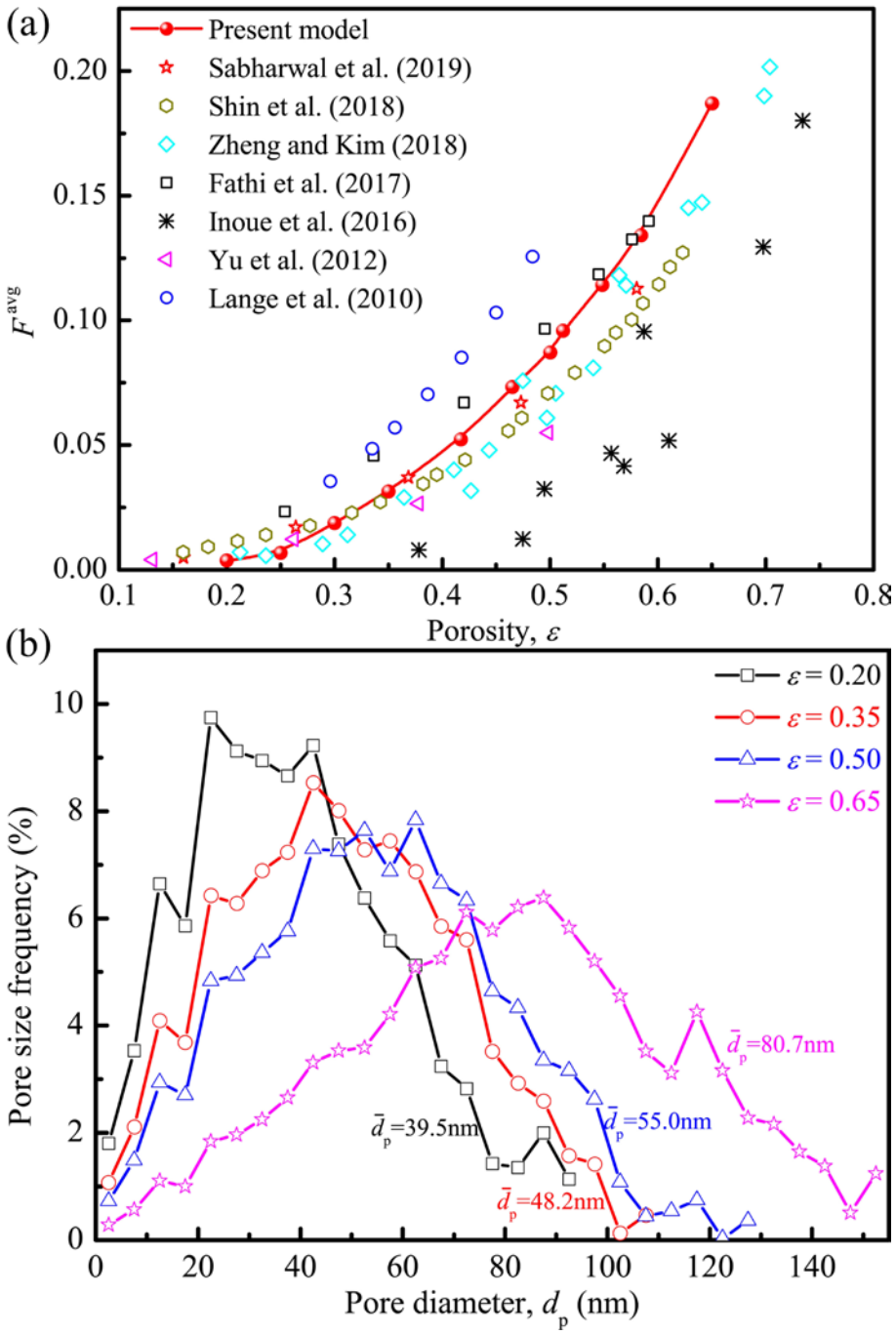

Fig. 4 Determination of the effective diffusivity in CL, (a) comparison of average formation factor F^{avg} for the stochastic reconstruction methods with existing studies [55-60]; (b) pore size distributions for different porosities

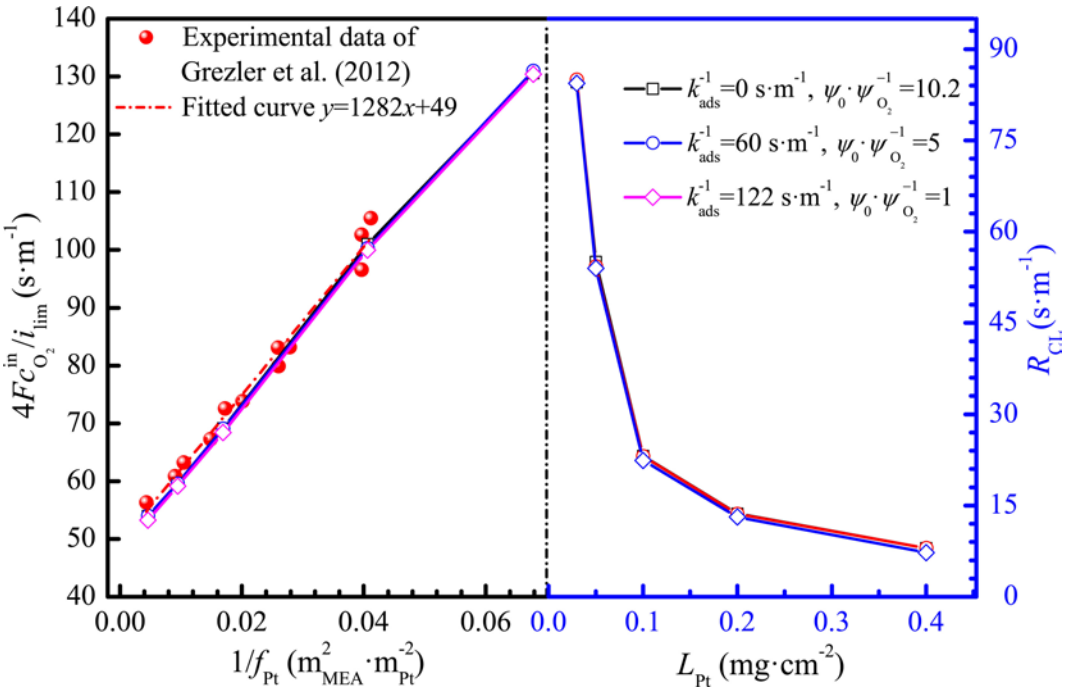

Fig. 5 Comparison of the total transport resistance versus f_{Pt}, and R_{CL} versus L_{Pt} between the experimental data [11] and the numerical predicted ones with three sets of model parameters

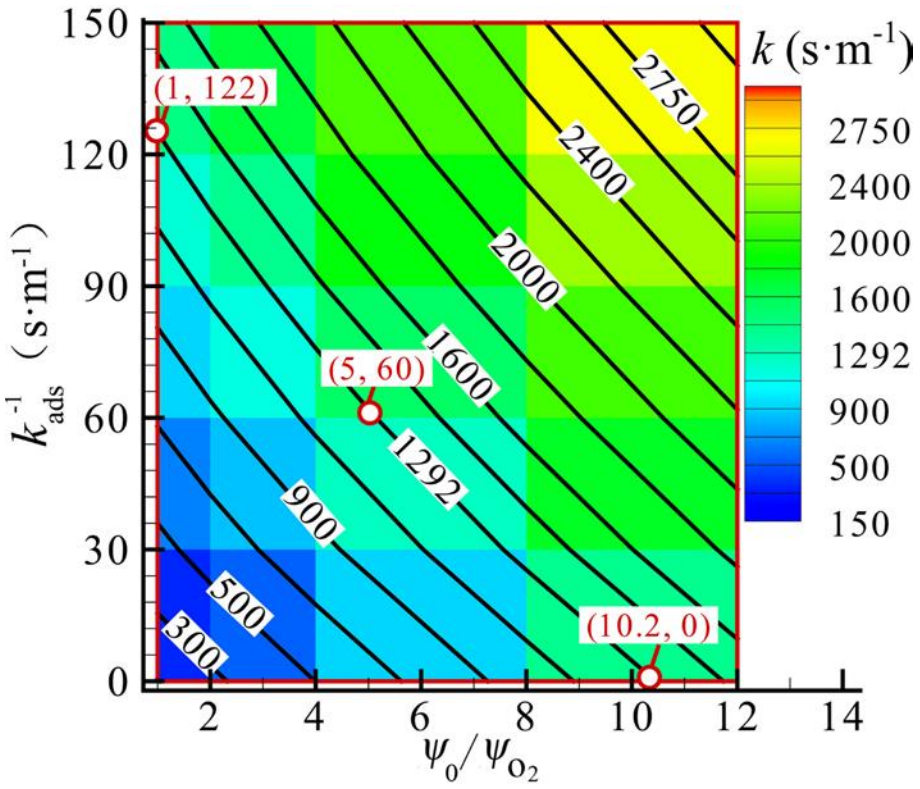

Fig. 6 Parameter sensitivity analyses of the adsorption rate k_{ads} and the ratio $\psi_0 \cdot \psi_{O2}^{-1}$ on the slope k

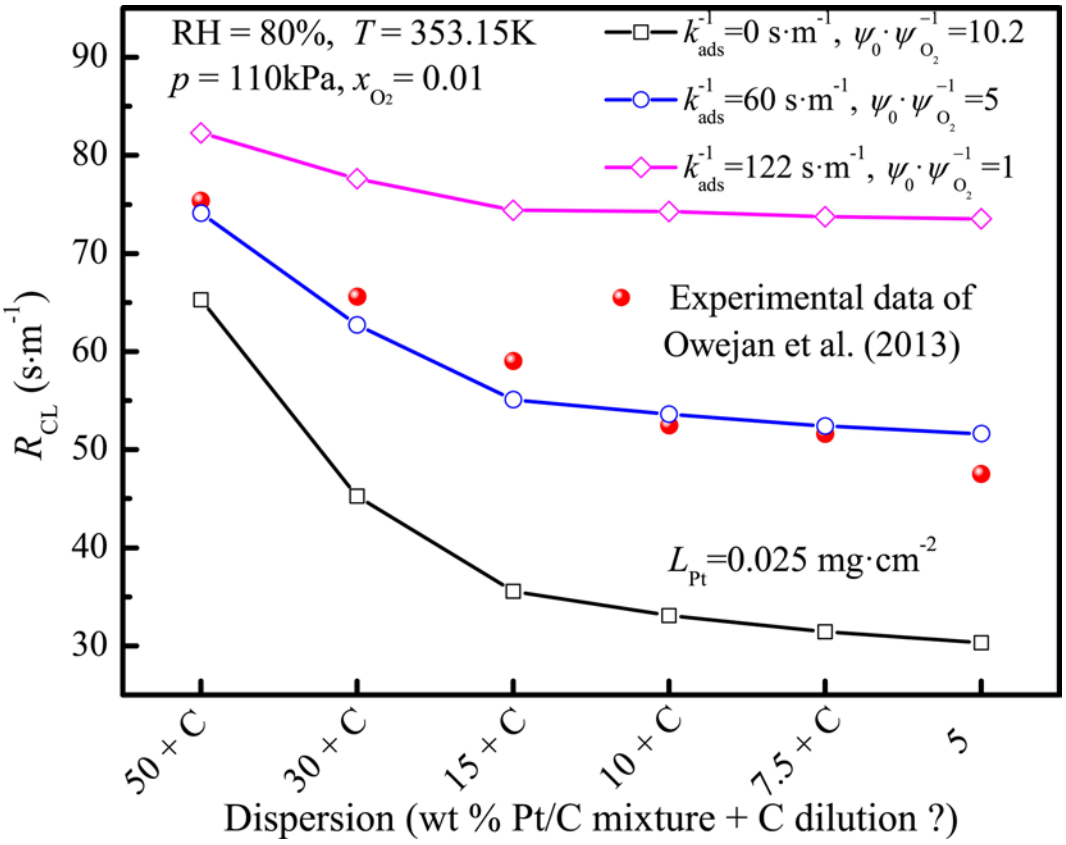

Fig. 7 Comparison of the impact of the carbon dilution on RCL between the experimental data [12] and the simulated ones with three sets of model parameters

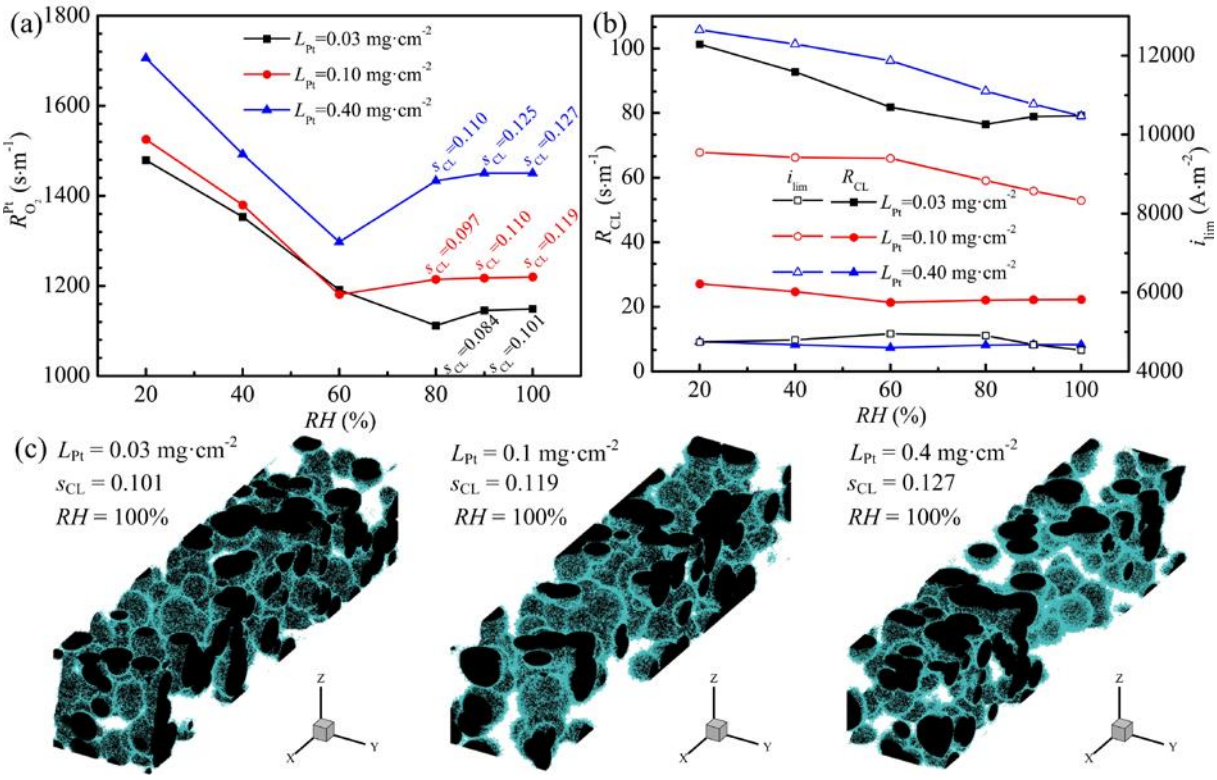

Fig. 8 Impacts of the relative humidity RH on the transport process in CL for three different L_{Pt}, (a) $R_{O_2}^{Pt}$ versus RH; (b) R_{CL} and i_{lim} versus RH; (c) snapshots of the liquid distributions for x ranging from 5.5 to 6.5 μm

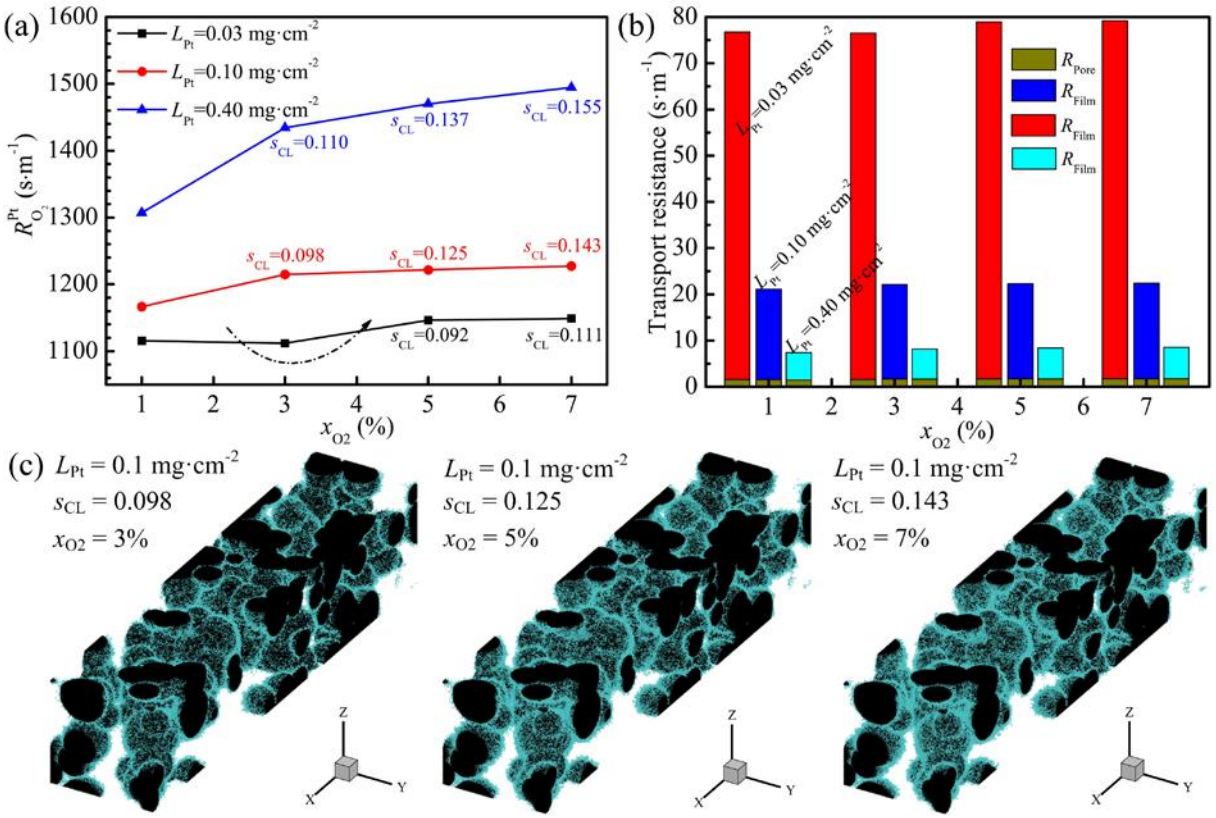

Fig. 9 Impacts of the oxygen molar fractions x_{O2} on the transport process in CL for three different L_{Pt}, (a) $R_{O_2}^{Pt}$ versus x_{O2}; (b) transport resistances versus x_{O2}; (c) snapshots of the liquid distributions for x ranging from 5.5 to 6.5 μm

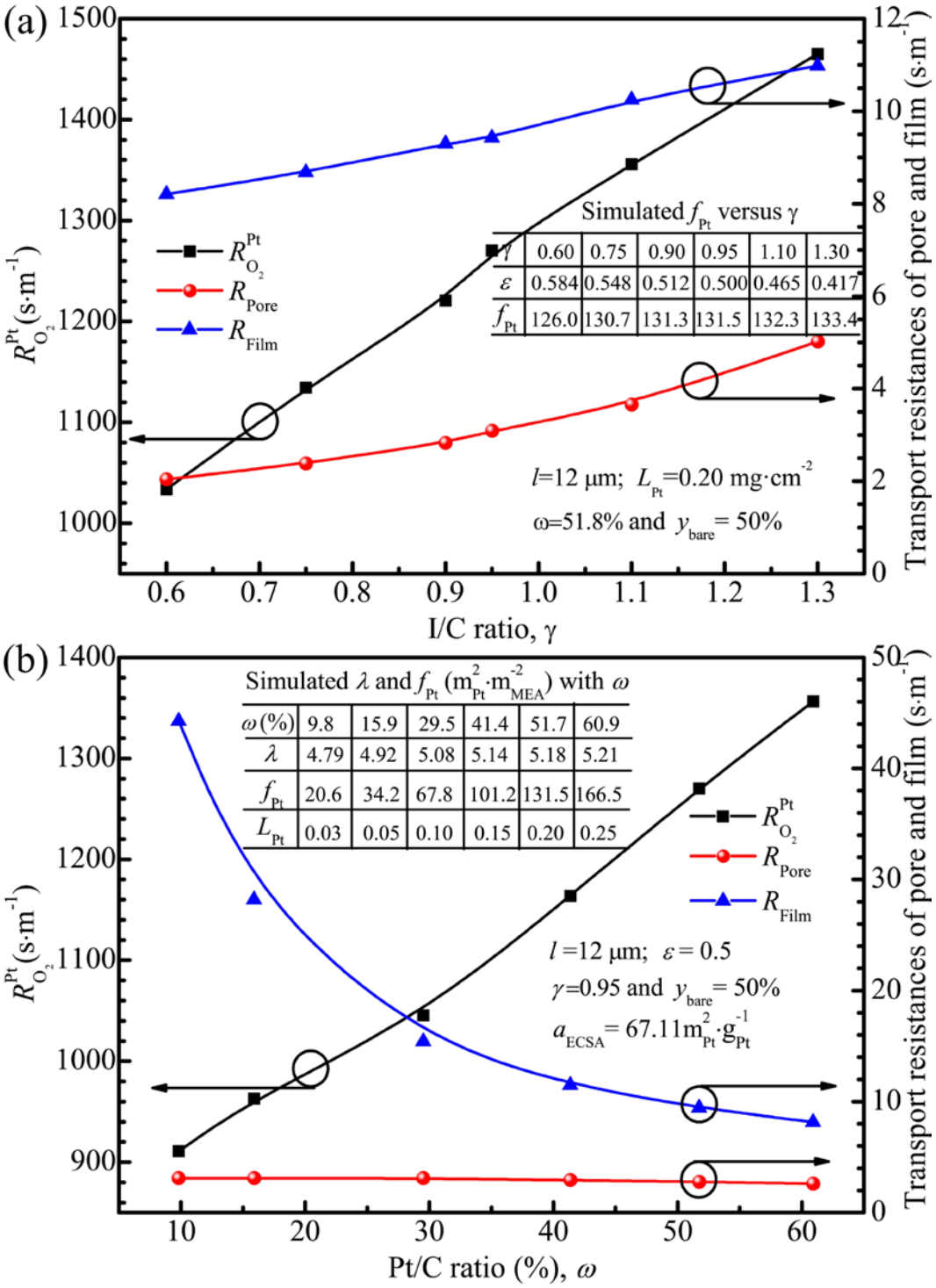

Fig. 10 Impacts of the structural parameters of CLs on the transport resistances, (a) I/C ratio γ for the structural parameters of l = 12 μm, L_{Pt} = 0.2 mg·cm^{-2}, ω = 51.8%, and y_{bare}=0.5; (b) Pt/C ratio ω for the structural parameters of l = 12 μm, $\sum$= 0.5, γ=0.95, and y_{bare}=0.5

Table Captions

Table 1. Structural parameters of the simulated cases

Table 2. Parameters for the electrochemical kinetics and the model [32, 38, 49]

Table 1

Structural parameters of the simulated cases

Case	L_{Pt} (mg□cm^{-2})	l (μm)	ε	γ	ω	y_{bare}
1	0.03	13.6	0.65	0.95	50%	0.93
2	0.05	13.6	0.65	0.95	50%	0.89
3	0.10	11.3	0.65	0.95	50%	0.72
4	0.20	12.7	0.65	0.95	50%	0.50
5	0.40	12.2	0.65	0.95	50%	0.00
6	0.025	11.0	0.53	0.95	5%	0.00
7	0.025	10.8	0.53	0.95	7.5%	0.34
8	0.025	10.7	0.53	0.95	10%	0.51
9	0.025	10.4	0.53	0.95	15%	0.69
10	0.025	11.3	0.53	0.95	30%	0.88

The cases numbered from 1 to 5 are based on Grezler's experimental work [11], and those numbered from 6 to 10 are based on Owejan's experimental work [12].

Table 2

Parameters for the electrochemical kinetics and the model [32, 38, 49]

Parameter	Value	Parameter	Value
$c_{O2,ref}$ (mol□m^{-3}) [49]	3.39	R (J□mol^{-1}K^{-1})	8.314
$D_{liq,O2}$ (m^2□s^{-1}) [32]	6.7×10^{-9}	α_c [38]	0.8
E_c (kJ□mol^{-1}) [38]	67	ρ_{liq} (kg□m^{-3}) [49]	970
EW (kg□mol^{-1}) [49]	1.1	ρ_{mem} (kg□m^{-3}) [49]	1980
F (C□mol^{-1})	96485	δ_{GDL} (μm)	200
H_{liq} (Pa□m^{-3}mol^{-1}) [32]	126252	δ_{mem} (μm)	40
j_0^{ref} (A□m^{-2}) [38]	0.3	σ (N□m^{-1}) [49]	0.0625
$k_{ion/liq,\ dis}$ (m□s^{-1})	□	$\theta_{CL/GDL}$ (°) [49]	95, 120
k_{ads} (m□s^{-1})	0.01667	μ_{liq} (kg□m^{-1}s^{-1}) [49]	3.51×10^{-4}
$K_{CL/GDL}$ (m^2) [49]	1×10^{-13}, 2×10^{-12}	ω_c (kJ□mol^{-1}) [38]	3.0